DIFFUSE REFLECTANCE SPECTROSCOPY AS A TOOL TO EVALUATE LIVER TISSUE

THERESE ALBURG & DAVID KRAUS

AUGUST 15, 2014

Master Thesis

LUND
UNIVERSITY

ABSTRACT

The shape of a diffuse reflectance spectra can provide knowledge about tissue composition. By analysing this spectra one can, with the right evaluation methods, find out information about the tissue. With known absorption properties of the present tissue chromophores it is possible, with a curve fit algorithm, to find their volume fractions in any measured tissue.

In this work, the usability of diffuse reflectance spectroscopy (DRS) as a tool in tissue diagnostics was investigated. A model based on diffusion theory with a semi-infinite boundary condition and known tissue chromophore data was developed. It was used to evaluate DRS signals in tissue phantoms and on murinae, porcine and human livers. To ease the evaluation, an interface was developed to run the instruments (one light source and two spectrometers) from the computer and to compute the tissue composition from the provided diffusion model. The tissue composition was computed through a Levenberg-Marquardt least-squares algorithm in MATLAB.

Validation of the diffusion model was performed on tissue phantoms together with Monte Carlo (MC) simulations and a Time-of-Flight Spectroscopy (TOFS) measurement. The results from the validation measurements were varying. Many different kinds of phantoms were created. Commonly used phantoms, containing water, blood and intralipid gave results systematically underestimating the absorption while phantoms with greater fractions of lipid, mixed with agar or Triton-X100, gave results with less good correlation between signals and concentrations. The poor phantom results were discovered to be due to a low haemoglobin concentration in the used blood whilst there was also limitations in the diffusion criteria for these phantoms.

The results from liver measurements gave better correlation between signals and concentrations, and when investigating the criteria for diffusion these were also fulfilled in a greater wavelength region. The liver results also showed an evident difference between healthy and malignant tissue.

POPULÄRVETENSKAPLIG SAMMANFATTNING

I dagens sjukvård finns det många etablerade metoder för att diagnostisera sjukdomar. Vissa av dessa är avbildningstekniker som PET, CT eller MR medan andra, som biopsi, är en annan typ av undersökning som utförs. Dessa metoder har både för- och nackdelar. Gemensamt för dem är att de antingen är dyra, potentiellt kan ha bieffekter eller tar lång tid. Sjukvården har många alternativ, men vilket är egentligen det bästa?

Optiska metoder är inte lika frekvent utnyttjade som diagnostiska verktyg. De är kraftfulla tekniker som varken gör skada, tar tid eller kostar mycket pengar. Genom att i stället använda sig av optiska metoder för diagnostik och terapi kan man både reducera kostnad, tid och i vissa fall förbättra den diagnostiska informationen. Självklart finns det inte endast positiva saker med de optiska metoderna, en stor nackdel är att ljuset inte når långt ner i vävnaden. Fotonerna når endast en bråkdel av en millimeter till någon centimeter ner i vävnaden, beroende på vilken färg ljuset har.

En optisk metod för att avgöra om viss vävnad är frisk eller skadad bygger på diffus reflektans. Genom att mäta den diffusa reflektansen på specifik vävnad kan man sedan räkna ut vilka komponenter som finns, samt till vilken grad de är närvarande. Detta tillsammans med kunskap om komposition om frisk samt skadad vävnad kan bidra till att ställa en diagnos.

Diffus reflektans har i det här projektet används till att karakterisera vävnad i levern. Applikationerna finns både genom att tekniken kan använadas som ett guidande hjälpmedel under kirurgi samt vid undersökning av kemoterapiskador. I den här rapporten beskrivs den underliggande teorin för hur ljus och vävnad växelverkar med varandra. Med detta som bakgrund har en modell för diffus reflektans utvecklats. Utifrån modellen valideras och evalueras instrument, i form av en optisk prob, en ljuskälla och två spektrometrar. Valideringen har också inkluderat metoder för att karakterisera levervävnad genom en fantomstudie samt genom mätningar på olika levrar. Modellen har också testats genom datorsimuleringar.

Valideringsmätningar av blodfantomerna gav varierande resultat vilket troligen berodde på låga hemoglobinvärden i blodet som användes samt begränsningar i diffusion teori. Levermätningarna gav bra resultat med en tydlig skillnad mellan hälsosam och sjuk vävnad.

CONTENTS

ACRONYMS

BMC BioMedical Center

CT Computed Tomography

DRS Diffuse Reflectance Spectroscopy

MC Monte Carlo

MCML Monte Carlo for Multi-Layered media

MR Magnetic Resonance

NA Numerical Aperture

NIR Near Infra-Red

PET Photon Emission Tomography

RTE Radiative Transport Theory

SNR Signal-to-Noise Ratio

TEC ThermoElectric Cooling

TOFS Time Of Flight Spectroscopy

UV Ultra Violet

VIS Visible

PARAMETERS

S_B	Hb oxygen saturation	%
B	Average blood volume fraction	%
W	Water volume fraction	%
L	Lipid volume fraction	%
Bi	Bile volume fraction	%
R	Average vessel radius	m
λ_o	Reference wavelength	nm
b	Scattering power (Mie slope)	-
a	Reduced scattering coefficient at the reference wavelength	m^{-1}
f_{Ray}	Fraction of Rayleigh scattering	-
n_t	Refractive index of tissue	-
n_f	Refractive index of optical fibre core	-
θ_c	Critical refractive angle	rad
ρ	Distance between optical fibres	m
μ_s	Scattering coefficient	m^{-1}
g	Anisotropy parameter	-
μ_s'	Reduced scattering coefficient	m^{-1}
μ_a	Absorption coefficient	m^{-1}
C_{diff}	Correction factor for inhomogeneously distributed absorbers	-
R_v	Vascular radius of blood vessel	m
μ_{eff}	Effective attenuation coefficient	m^{-1}
μ_t	Total attenuation coefficient	m^{-1}
D	Diffusion coefficient	m
a'	Transport albedo coefficient	-
R_0	Specular reflectance	-
A	Coefficient compensating for refractive index mismatch when handling the boundary condition in diffusion	-
z_b	Extrapolated boundary	m
z_o	Subsurface depth of isotropic photon source	m
r_1	Distance: light source-detector	m
r_2	Distance: image source-detector	m
R_d	Diffuse reflectance	%

1 INTRODUCTION

The first chapter will give a short introduction to a few optical imaging techniques; with focus on DRS, which is the technique used in this thesis. The outline of the thesis: with its purpose, aims and assumptions are also stated.

1.1 OPTICAL IMAGING

Optical imaging techniques involves ultraviolet (UV), visible (VIS) and/or near-infrared (NIR) light. As light propagates in turbid media, photons will either scatter: stray from their path, or be absorbed: converted to heat. These two properties depend on the specific medium in which they are traveling. Scattering and absorption are wavelength dependent properties and they can be used to model light propagation in a medium. These properties can also provide information about the medium itself.

Light of wavelengths ranging between 600 - 1400 nm is less attenuated in tissue, and this range is thus called the tissue optical window. It is optimal to use light in this wavelength range in optical measurements of subsurface tissue structures. However, the penetration depth of light is still limited to sub-centimeter range at best. In this region, optical techniques have a high sensitivity, and could in theory determine the structure and constitution of the imaged sample.

There are many biomedical imaging techniques using light, e.g. DRS (this work), diffuse optical tomography [1], fluorescence imaging [2], bioluminescence imaging [3] and many more. With light penetration only being in the millimeter to centimeter scale, one cannot measure something buried deep into the tissue. However, optical techniques show great potential, as they are much cheaper and require a relatively primitive setup compared to other available techniques, such as PET/CT. Also, the optical techniques are not harmful to those working with it or those seeking a treatment or diagnosis.

1.2 DIFFUSE REFLECTANCE SPECTROSCOPY

DRS is a widely used non-invasive technique for optical imaging. The fact that DRS can be used to measure without destroying or affecting samples makes the technique ideal to use in a number of applications. These applications can be used in several fields, e.g. the food industry [4], the drug industry [5, 6] and as an optical tool for diagnostics and analysis within medicine [7, 8].

DRS and tissue chromophore detection

In the field of tissue chromophore detection, i.e. detection of water, blood, etc., DRS has been used to diagnose cancer in breast [9, 10], colon [11] and more. A DRS setup usually consist of two or more optical fibres. The fibres are most commonly placed parallel and fixed in a pen-like probe [12]. By acquiring the diffuse reflectance of light from tissue, a diffuse reflectance spectrum can be obtained. The spectrum contains information about the medium, such as the optical properties and the structure. This information can be used to get an overview of what the tissue is composed of through various models.

Several groups work with DRS and the most common wavelength range used is 500 - 1000 nm. However, lately it has been shown that if the wavelength range is increased up to 1600 nm a more trustworthy and robust result can be obtained [13].

1.3 PURPOSE

The purpose of this thesis is to validate a DRS setup. This setup should be able to assist tumour resection in liver surgery, especially for patients that has undergone chemotherapy prior to the surgical resection. The evaluation is performed through an inverse model of the diffusion theory, following proper method validation by measuring the diffuse reflectance in tissue-like phantoms with an optical probe. Then, through a curve fitting algorithm, one can determine the optical properties of the tissue and concentrations of chromophores. A computer program with a simple interface is also desired for the DRS setup to function in an environment used by non-technicians, such as nurses or doctors.

1.4 SPECIFIC AIMS

The primary aim of this thesis is to create a tool to determine if a liver is healthy, unhealthy or how it is responding to chemotherapy. The work is directed to establish the correlation between the diffused reflectance (i.e. the signal) and chromophore composition in tissue. The specific aims are to:

A. Validate the system

B. Implement a working curve fit algorithm

C. Design a program that is acceptable to work with, by those whom it may concern

D. Establish diagnostic criteria to differentiate healthy and malignant tissue through DRS

E. Investigate the relationship between probe pressure on tissue and the shape of recorded diffuse reflectance spectra

F. Evaluate the limitations of diffusion theory

1.5 ASSUMPTIONS

In this thesis the following assumptions are made

- Tissue compositions make light diffuse. This assumes that the scattering coefficient is considerably larger than the absorption coefficient ($\mu_s' >> \mu_a$) and that the fibre separation is greater than the reciprocal of the scattering ($\rho > 1/\mu_s'$).
- The short fibre separation in some of the probes are used without respect to the limitations in the diffusion theory.
- The angle of incident light is set to 0°. The diffusion model is dependent on the angle of incidence; when measuring in practice the actual angle is not well characterised.
- The temperature dependences of light absorption and scattering by various chromophores and microscopic structures of elements are neglected, i.e. $\mu_s^{'}$ and μ_a are assumed to be independent of the temperature.
- Intralipid, used as a scattering agent, is assumed to absorb light similarly to water and modeled as water in the curve fit.

2

THE LIVER

The technology in this thesis has applications for liver metastasis and the livers reaction to chemotherapy. Therefore, this chapter contains a brief introduction to the liver and the medical problem of relevance for the work in this thesis.

2.1 DISEASES IN THE LIVER

The liver is one of the most vital organs in our body and we cannot survive without it. It is situated to the right of the stomach and overlies the right kidney and the gallbladder, see Figure 2.1. The liver receives the majority of its blood, 75 %, from the hepatic portal vein which runs from the gastrointestinal tract through the spleen to the liver [14].

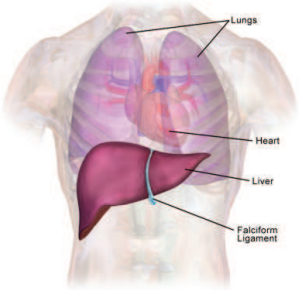

Figure 2.1: Placement of liver in human body. (Image extracted from Wikimedia, "Liver location", 02-06-2014)

Malignant tumours in organs in the gastrointestinal tract, such as esophagus, stomach, biliary system, pancreas, small intestine and large intestine, are categorised as gastrointestinal cancer. This form of cancer make up 10 % of all malignant diseases, the third most common malignancy, among both men and women [15].

Since the liver's blood supply runs through the gastrointestinal tract the liver is highly receptive to metastatic growth. A metastatic tumour, or metastasis, is the spread of malignant tumour cells across tissue boundaries whilst a primary tumour is the first original tumour in a body. A metastatic tumour in the liver is 4 - 5 times more common than a primary tumour [16].

2.2 TREATMENT OPTIONS

There are several treatment options of metastatic liver lesions: the most common being chemotherapy, radiofrequency ablation, and surgery [17]. Some of these can be combined, like chemotherapy and surgery. Surgery involves a major operation, which is usually reserved for those with good health, and is the only therapy with a possibility of curing the patient [18]. The resected part can make up as much as 80 - 90 % of the liver, due to it's remarkable ability to regenerate [19].

Pre-operative chemotherapy and it's consequences

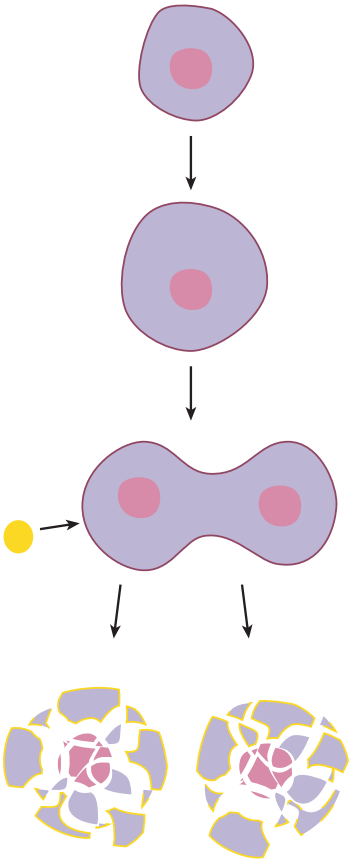

Figure 2.2: The chemotherapeutic drug (yellow) attack cells as they are dividing.

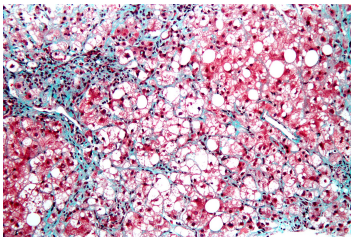

Figure 2.3: Liver with steatohepatitis. (Image extracted from Wikimedia, "Steatohepatitis", 02-06-2014)

Chemotherapy, abbreviated chemo, is one of the more commonly used means to treat cancer today [17]. When malignant cells are spread out, chemotherapy can be used to kill these cells and also to reduce the weight of the tumour. These two elements enable the patient to undergo surgery.

Chemotherapy is essentially a chemical substance injected into the body of patients [20]. When in the body, it will locate cells in the process of dividing and eradicate them, see Figure 2.2. For the best result, the chemotherapeutic drug should only be attracted towards the malignant cells and leaving the healthy ones undamaged.

Malignant cells constantly divide and multiply and grow into a lump with time, often referred to as a tumour. Most, but not all, normal cells divide less frequent after you reach adulthood. Normal cells which still has a high multiplication frequency include:

- Hair cells - the hair is constantly growing.
- Blood cells - the cells are invariably being produced within the bone marrow.
- Skin and digestive lining cells - both are renewed frequently.

These cells are also highly susceptible to the chemotherapy [21].

Studies show that the use of pre-operative chemotherapy can induce other consequences than destroying healthy cells. Pre-operative chemotherapy increases the risk of several fatty liver conditions, such as: steatosis, steatohepatitis (Figure 2.3) and sinusoidal obstruction syndrome [22]. Diagnosing these symptoms either involve a liver biopsy; where a piece of liver tissue is extracted and examined, or various other diagnostic techniques, such as ultrasound, CT or MR. Although the latter ones are non-invasive, they are expensive and have low sensitivity for these conditions, thus provide limited diagnostic information. Ultrasound is the least expensive of these techniques, but also offers the lowest sensitivity [23].

2.3 DRS

By using a DRS setup, mentioned in Chapter 1, a higher sensitivity is possible to achieve. With this technique, a surgeon can hopefully detect pre-operative chemotherapy induced injuries on the liver. These fatty liver conditions cannot be seen by the naked eye, which makes DRS a suitable technique to adopt. A DRS probe can measure, while in contact with the liver surface, during open

surgery. This technique can help to establish the state of the liver segment which will remain in the body after surgery. Diagnosing fatty liver conditions with the DRS-technique is a novel idea still to be evaluated, with a potential to develop as a clinical diagnostic application during open liver surgery.

DRS is not a time consuming technique, a single acquisition only takes a few seconds. The surgeon would also have the choice of someone watching and analysing the data in real-time or save the data and perform the analysis at a point later in time. Potentially an online real-time evaluation can be developed in the future. The theory and use the use of DRS will be discussed in Chapter 3 and Chapter 4.

3

LIGHT-TISSUE INTERACTION

When light is propagating in tissue, it is either scattered or absorbed. The coefficients describing these two processes are, together with the refractive index, called the optical properties of the tissue. In the following chapter the theory of scattering, absorption and the radiative transport equation (RTE) will be described as well as the diffusion equation, as an approximate solution to the RTE.

3.1 SCATTERING

When a medium is inhomogeneous (here meaning the refractive index is spatially varying on a microscopic scale), light will scatter as it propagates. The scattering of light in a medium can be described by the scattering coefficient (μ_s), defined as the average number of scattering events per unit length. However, to fully describe scattering in tissue more information than this is needed. For the description to become more accurate the change in direction of the light should also be considered.

The probability of a photon to scatter from the direction s' to s is described by the scattering phase function ($p(\mathbf{s}, \mathbf{s'})$), illustrated in Figure 3.1. The scattering phase function depends on the angle (θ) between two scattering events and is often approximated by the Henyey-Greenstein phase function [24]

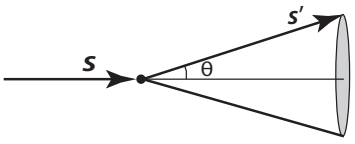

Figure 3.1: The phase function of single scatter, $p(\mathbf{s}, \mathbf{s'})$.

$$p(\theta) = \frac{1}{4\pi} \cdot \frac{1 - g^2}{(1 + g^2 - 2 \cdot g(\cos\theta))^{\frac{3}{2}}}, \tag{1}$$

where g is the anisotropy factor, defined as the average of the cosine of the scattering angle

$$g = \langle \cos(\theta) \rangle, \tag{2}$$

with $g = 1$ being completely forward scattering and isotropic scattering characterised with $g = 0$. Both the scattering coefficient and the anisotropy factor are wavelength dependent.

With the anisotropy factor we can define a reduced scattering coefficient as

$$\mu_s' = \mu_s \cdot (1 - g). \tag{3}$$

Finding the true value of the reduced scattering at all wavelengths through Equation 3 can be difficult. However, the reduced scattering can be approximated by a power law. In literature, two ways of describing the scattering coefficient are commonly used [25]. One can either describe the scattering as Mie-scattering and the power law takes the form

$$\mu_s'(\lambda) = a \cdot \left(\frac{\lambda}{\lambda_0}\right)^{-b}, \tag{4}$$

where λ_0 is the reference wavelength, which in this project is set to 800 nm, a the reduced scattering at λ_0 and b is the scattering power.

As an alternative the reduced scattering coefficient can be described as a function of both Mie- and Rayleigh-scattering

$$\mu_s'(\lambda) = a \cdot \left[f_{\text{Ray}} \left(\frac{\lambda}{\lambda_0}\right)^{-4} + (1 - f_{\text{Ray}}) \left(\frac{\lambda}{\lambda_0}\right)^{-b} \right], \tag{5}$$

where a and b are defined as above and f_{Ray} is the fraction of Rayleigh scattering. Rayleigh scattering is caused by particles much smaller than the wavelength of light, while particles which are similar to or larger in size are described by Mie scattering. For the entire wavelength range, 400 - 1600 nm, it is not established which of Equation 4 or Equation 5 models the scattering the most accurate [25], so in the presented model both options will be considered.

3.2 ABSORPTION

When light is propagating in tissue it can also be absorbed. The absorption of light depends on the chromophores in the tissue. The absorption coefficient (μ_a) is defined in a similar way to the scattering coefficient, i.e. the probability for a photon to get absorbed per unit length. The ratio of the chromophores present in tissue will determine how the absorption spectra will look, since the absorption coefficient is the linear combination of the contribution of each of the absorbing chromophores [25]

$$\mu_a(\lambda) = \sum_i \mu_{a,i}(\lambda) \cdot f_i, \tag{6}$$

where $\mu_{a,i}$ is the absorption coefficient for chromophore i and f_i is the volume fraction of that corresponding chromophore.

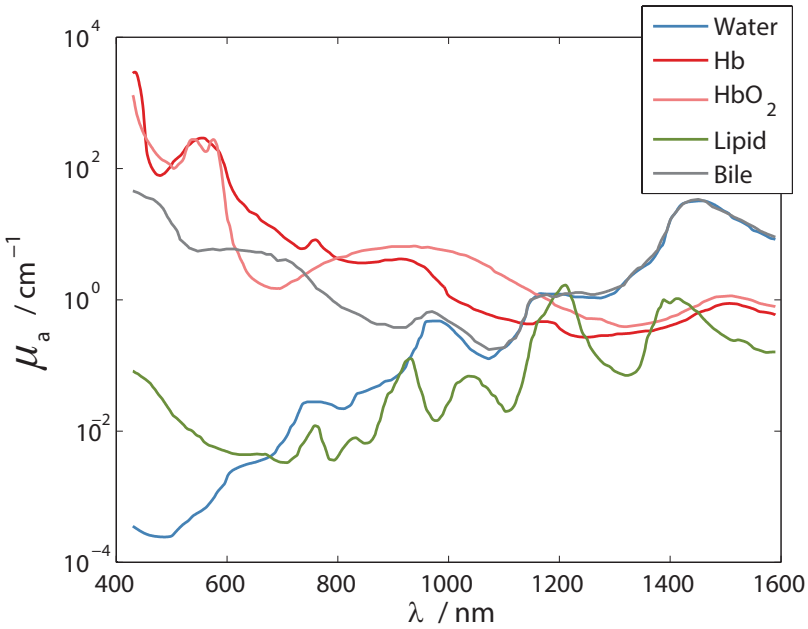

Figure 3.2: Absorption coefficients (μ_a) as a function of wavelength (λ) for the main chromophores present in the liver [26]. The tissue optical window ranges from ~600 - 1400 nm and is the region in which the chromophores absorb the least, hence light will reach deeper into the tissue.

The strongest absorbers in biological tissue are blood, water and lipids. For liver applications, bile should also be taken into account [26]. Blood consists of red blood cells (~45.0 %), white blood cells (~0.70 %), platelets and plasma (~54.3 %). Of these, the greatest absorber, and also the greatest contribution to scattering, are the red blood cells; these cells contain primarily haemoglobin.

Haemoglobin can be both oxygenated and deoxygenated, thus the oxygenation of blood should be accounted for when modeling light propagation. The ratio between oxygenated and total haemoglobin, the oxygen saturation (S_B), is [HbO_2]/[HbO_2 + Hb] with HbO_2 as fully oxygenated haemoglobin and Hb as fully deoxygenated haemoglobin. The oxygenation saturation ranges from ~75 % in venous blood to ~97.5 % in arterial blood [27].

The described chromophores will yield the total absorption coefficient as follows

$$\mu_a = B \cdot [S_B \cdot \mu_a^{HbO_2} + (1 - S_B) \cdot \mu_a^{Hb}] + W \cdot \mu_a^{H_2O} + L \cdot \mu_a^{Lipid} + Bi \cdot \mu_a^{Bile}, \tag{7}$$

where S_B is the oxygenation saturation, while B, W, L and Bi are the volume fractions of blood, water, lipids and bile, respectively.

The absorption coefficients as a function of wavelength for these chromophores can be viewed in Figure 3.2.

Pigment packing

Equation 7 assumes all chromophores to be homogeneously distributed in tissue, however, this is not always true. To compensate for the inhomogeneous distribution of blood, i.e. that blood is concentrated in blood vessels, a correction factor can be taken into account. This is called pigment packing and was suggested in reference [28]. If the blood vessel radius (R_v) is large, less light will reach through the vessel. As a consequence, the measured absorption coefficient will be smaller than its true value, since the model assumes blood to be homogeneously distributed. The correction factor (C_{diff}) for blood vessels exposed to diffused light is

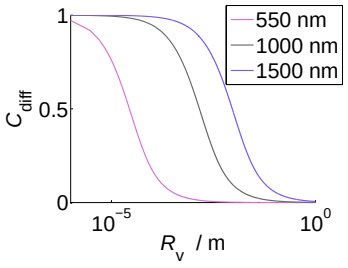

Figure 3.3: Correction factors (C_{diff}) for inhomogeneously distributed absorbers as a function of the vessel radius (R_v) for the absorption coefficient (μ_a^{blood}) in blood calculated at three different wavelengths.

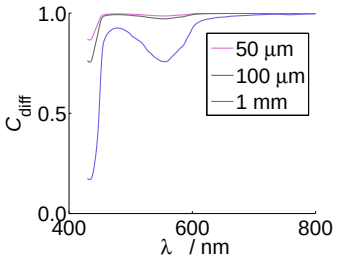

Figure 3.4: The correction factor (C_{diff}) as a function of the absorption coefficient (μ_a^{blood}) in blood for three different vessel radii (R_v). For wavelengths over 800 nm the value for C_{diff} stays at ∼1.

$$C_{diff}(R_v, \mu_a^{blood}(\lambda)) = \frac{1 - e^{-2 \cdot R_v \cdot \mu_a^{blood}(\lambda)}}{2 \cdot R_v \cdot \mu_a^{blood}(\lambda)}, \tag{8}$$

where R_v is the vascular radius of the blood vessel and μ_a^{blood} the absorption coefficient of blood [28]. The correction factor is close to one for small vessel optical density ($R_v \cdot \mu_a^{blood}$) and decreases the as the optical density increases, see Figure 3.3. In Figure 3.4 one can notice that pigment packing has a greater effect for shorter wavelengths.

The new, corrected, expression for the absorption coefficient can be expressed as

$$\mu_a^{tissue} = C_{diff} \cdot B \cdot [S_B \cdot \mu_a^{HbO_2} + (1 - S_B) \cdot \mu_a^{Hb}] + \sum_i f_i \cdot \mu_{a,i}, \tag{9}$$

where μ_a^{tissue} is the effective absorption coefficient for tissue, $\mu_a^{HbO_2}$ the absorption coefficient of fully oxygenated blood, μ_a^{Hb} fully deoxygenated blood, S_B the oxygen saturation and B the blood volume fraction as in Equation 7.

Beer-Lambert Law

The Beer-Lambert law describes how the intensity of light passing through an absorbing media decreases exponentially on the product of the absorption coefficient and the path length

$$I = I_0 \cdot e^{-(\mu_a \cdot l)}, \tag{10}$$

where I is the transmitted intensity, I_0 the incident light and l the optical path length in the medium. For a non-scattering medium the optical path length is equal to the sample thickness. For a scattering medium the attenuation of the light can be expressed as

$$I = I_0 \cdot \frac{1}{r} \cdot e^{-(\mu_{\text{eff}} \cdot r)}, \tag{11}$$

where r is the geometrical distance and μ_{eff} is the effective attenuation coefficient depending on both absorption and scattering.

3.3 TEMPERATURE DEPENDENCE FOR OPTICAL PROPERTIES

Both the scattering and the absorption coefficients are temperature dependent. Chromophores absorb differently for different temperatures. The temperature dependence of water absorption has been studied; the absorption peak around 970 nm blue-shifts for higher temperatures and the absorption peak also gets more narrow and stronger [29, 30]. However, these changes are usually negligible in biomedical optical applications. Small temperature variations should not affect the diffuse reflectance spectrum significantly.

The temperature dependence of the scattering coefficient is related to the refractive index. The refractive index is temperature dependent, which in turn makes the scattering coefficient temperature dependent as well. Also, lipids may undergo a phase transition between room and normal body temperature, drastically altering scattering properties of tissue.

3.4 PROBE-TISSUE CONTACT STATE

The contact state between probe and tissue influences the shape of the diffuse reflectance spectra. The contact state can be the pressure the probe is inducing on the tissue, see Figure 3.5. The signal will also depend on which angle the probe is held, as shown in Figure 3.6. For light pressures the reflectance is expected to be greater, but take the same form. For greater pressures deformation of the tissue will take place and the expected shape of the curve will be changed. The measured intensities, in the spectra, will change differently depending on which wavelength is studied and these changes can affect the performance of the evaluation of the data. Some theories say that the induced pressure compresses the blood vessels and therefore influences the blood flow which will alternate the shape and strength of the obtained signal [31].

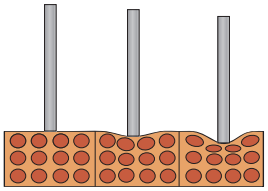

Figure 3.5: Different pressures in the contact state between the probe and tissue will affect the tissue structure and the shape of the acquired spectra.

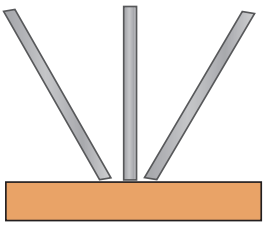

Figure 3.6: Different angles with which the probe is held will affect the shape of the acquired spectra.

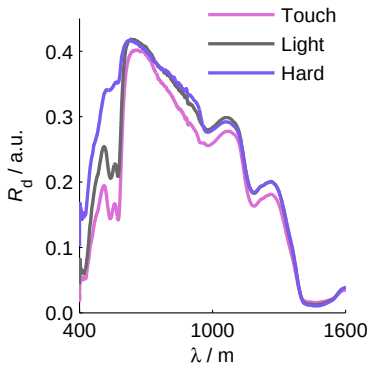

Figure 3.7: Diffuse reflectance (R_d) as a function of wavelength (λ) for experimental values for different pressures against a finger.

Different behaviour of the shape of the acquired spectra has been noticed by several groups [32, 33, 34, 35]. Wavelengths below 600 nm increase in diffuse reflectance intensity and wavelengths above 600 nm an applied pressure gives a decrease in diffuse reflectance, see Figure 3.7. Some investigators have also observed a pivot pattern around 590 nm, which would verify this [32].

3.5 RADIATIVE TRANSPORT THEORY

When modeling light propagation in tissue, with known optical properties, the RTE can be used. The RTE is complicated to solve without approximations. In this thesis, the RTE is modeled through the diffusion approximation and through MC simulations. MC is considered the gold standard for these problems.

The quantity used to describe propagation of photon power in tissue is called radiance ($L(\mathbf{r}, \hat{\mathbf{s}}, t)$). It is defined as power per area per solid angle. The photon distribution function ($N(\mathbf{r}, \hat{\mathbf{s}}, t)$) is the number of photons within a volume with a certain direction at a certain time. Radiance is the photon distribution multiplied by the photon energy ($h \cdot v$) and the speed of light (c),

$$L(\mathbf{r}, \hat{\mathbf{s}}, t) = N(\mathbf{r}, \hat{\mathbf{s}}, t) \cdot hvc. \tag{12}$$

The RTE is derived in a small element with volume V and boundary S, see Figure 3.8. When deriving the RTE the conservation of energy, absorption and scattering of photons and a photon source within the element are considered. The RTE is

$$\int_V \frac{\partial N}{\partial t} dV = -\underbrace{\int_S cN\hat{\mathbf{s}} \cdot \hat{\mathbf{n}} dA}_{\text{a)}} - \underbrace{\int_V c\mu_a N dV}_{\text{b)}} - \underbrace{\int_V c\mu_s N dV}_{\text{c)}} + \underbrace{\int_V c\mu_s \int_{4\pi} p(\hat{\mathbf{s}'}, \hat{\mathbf{s}}) N(\hat{\mathbf{s}'}) d\omega' dV}_{\text{d)}} + \underbrace{\int_V q dV}_{\text{e)}}, \tag{13}$$

where c is the speed of light, and q is the source term [36].

In clinical applications the fluence rate often has more significance than the radiance. The fluence rate is defined as the integral of the radiance over all directions

$$\psi(\mathbf{r}, t) = chv \int_{4\pi} N(\mathbf{r}, \hat{\mathbf{s}}, t) d\omega, \tag{14}$$

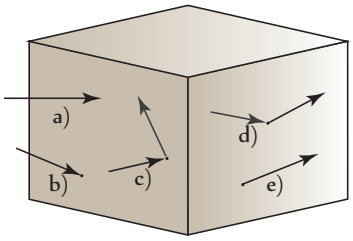

Figure 3.8: RTE in a small element with volume V and boundary S.
a) Transfer of photons across the boundary
b) Loss due to absorption
c) Loss due to scattering
d) Gain due to scattering
e) Photons generated by a source

hence we can compute the absorption of a photon independently of its direction.

3.6 DIFFUSION THEORY

In this work, a diffusion model was developed as an approximation of the RTE. The solution was developed for the steady state diffuse reflectance, in order to solve for the composition of the chromophores in terms of volume fractions. The diffuse reflectance (R_d) is a function of the distance between the emitting and collecting fibre (ρ), the absorption and the scattering coefficients. The distance between the fibres is a fixed value depending on probe geometry, see Chapter 4.

The model was constructed to be valid for liver tissue and thus for the chromophores present in the liver. There are variations in the composition of tissue from individuals and from healthy and unhealthy tissue. Variation can also be found for the same individual at different occasions.

The propagation of light in the tissue was approximated with the diffusion equation as previously by Farrell et. al. [37]

$$\nabla^2\psi(\mathbf{r}) - \frac{\mu_a}{D}\psi(\mathbf{r}) = -\frac{S_0(\mathbf{r})}{D} + 3\nabla \cdot S_1(\mathbf{r}), \tag{15}$$

where $S_o(\mathbf{r})$ and $S_1(\mathbf{r})$ are the zeroth and first order spherical harmonics and D is the diffusion coefficient which can be either $[3(\mu_a + \mu_s')]^{-1}$ or $[3\mu_s']^{-1}$. Since the scattering is assumed greater than the absorption, μ_a is sometimes neglected from the expression for the diffusion coefficient.

For a semi-infinite medium the boundary condition for the diffusion equation is approximated by

$$\psi(\mathbf{r}) - 2AD\hat{\mathbf{n}} \cdot \nabla\psi(\mathbf{r}) = 0, \tag{16}$$

where $\hat{\mathbf{n}}$ is a unit normal vector with direction into the tissue and A is a factor related to the internal reflection and the refractive indices (n) on the boundary

$$A = \frac{2/(1 - R_0) - 1 + |\cos\theta_c|^3}{1 - |\cos\theta_c|^2}, \tag{17}$$

where $\cos\theta_c$ is the critical refractive angle and R_0 the specular reflectance. R_0 is dependent on the refractive index in the tissue (n_t) and in the optical fibre (n_f) in the following way

$$R_0 = \left[\left(\frac{n_t}{n_f} - 1\right) / \left(\frac{n_t}{n_f} + 1\right)\right]^2. \tag{18}$$

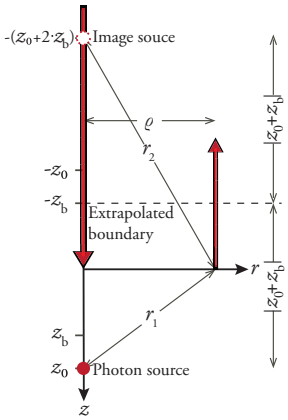

Figure 3.9: Geometry of the diffusion equation with the modeled boundary conditions.

To fulfill the boundary condition, the model assumes an isotropic light source at the distance one mean free path from the tip of the optical fibre, which is the location of the first scattering site in the tissue. Then a negative image source is introduced to set the fluence at an extrapolated boundary equal to zero. The location of the extrapolated boundary depends on both the diffusion coefficient and the factor A. The diffuse reflectance was solved from Equation 15 and the boundary condition from Equation 16, which is the geometry illustrated in Figure 3.9 for two different light sources [37]. The single source approximation is

$$R(\rho, \mu_s'(\lambda), \mu_a(\lambda)) = \frac{a'}{4\pi}\left[\frac{1}{\mu_t}\left(\mu_{eff} + \frac{1}{r_1}\right)\frac{e^{-\mu_{eff} r_1}}{r_1^2} + \left(\frac{1}{\mu_t} + 2z_b\right)\left(\mu_{eff} + \frac{1}{r_2}\right)\frac{e^{-\mu_{eff} r_2}}{r_2^2}\right], \tag{19}$$

where the source is an exponential line source, and secondly the extended source approximation is

$$R(\rho, \mu_s'(\lambda), \mu_a(\lambda)) = \frac{1}{4\pi}\left[\frac{1}{\mu_t}\left(\mu_{eff} + \frac{1}{r_1}\right)\frac{e^{-\mu_{eff} r_1}}{r_1^2} + \left(\frac{1}{\mu_t} + 2z_b\right)\left(\mu_{eff} + \frac{1}{r_2}\right)\frac{e^{-\mu_{eff} r_2}}{r_2^2}\right], \tag{20}$$

where the source models multiple buried sources along the z-axis whose contributions are integrated and calculated at the surface [37]. The two expressions differ only in the transport albedo (a'). In Equation 19 and Equation 20, z_b is the location of the extrapolated boundary located at $2AD$, z_0 the location of the isotropic photon source, z the distance between the probe and the tissue during the measurement. r_1 is the distance between the real light source and the detector, r_2 is the distance from the image source to the detector and ρ is the distance between the illuminating position and collecting fibre. $\mu_t = \mu_s' + \mu_a$ is the total attenuation coefficient, $a' = \mu_s'/\mu_t$

the transport albedo, and finally $\mu_{\text{eff}} = [3\mu_a(\mu_a + \mu_s')]^{1/2}$ the effective attenuation coefficient.

The scattering coefficient, diffusion coefficient and the light source can all be described through two different sets of equations. The diffusion model can thereby be written through eight combinations of these equations.

Limitations with diffusion theory

Since the diffusion model is an approximation to the RTE, it has some limitations. For the model to be valid the scattering needs to be much greater than absorption, i.e. $\mu_s' >> \mu_a$. In tissue, blood is highly absorbing around ~400 nm and above 1000 nm lipids and water are absorbing. In these regions this criteria might not be met. Furthermore, the distance between the emitting and collecting fibre (ρ) also limits the diffusion model. The distance needs to be great enough for the light to get diffused, this means that $\rho > 1/\mu_s'$, if the fibre separation is not long enough diffusion is not a good approximation.

Penetration depth

The depth of light penetration in a medium is dependent on the absorption and scattering coefficients, further it is also dependent on the fibre separation. The penetration depth is a measure of how deep photons can travel and still be detected at the tissue surface. In Figure 3.10 a schematic picture of light penetration is presented. As shown in the illustration not all depths are of equal probability.

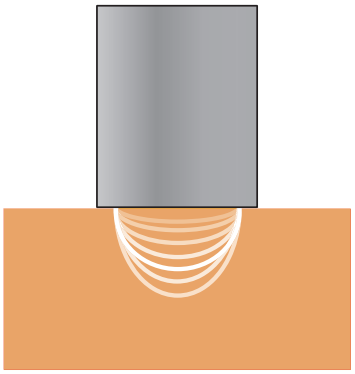

Figure 3.10: For a given fibre separation one penetration depth will be more likely than others.

The dependency of absorption is simple - higher absorption equals less light and vice versa. However, the detected amount of photons have a different dependency considering scattering. With little or no scattering, the light will pass through the medium and no diffused light is detected. With increased scattering, a direction change of a photon is more likely and this is consistent with a higher diffuse reflectance up till a breaking point where it will start to decrease. This can be shown in the diffusion model for a fixed fibre distance [38].

As stated above, the penetration depth is also dependent on the fibre separation. For a short separation, a high signal is achieved but the light is probing a small volume. By extending the fibre distance, a larger volume is probed, with the trade-off of a weaker signal. In the case of studying tissue, a greater volume is usually desired to get a more homogeneous picture.

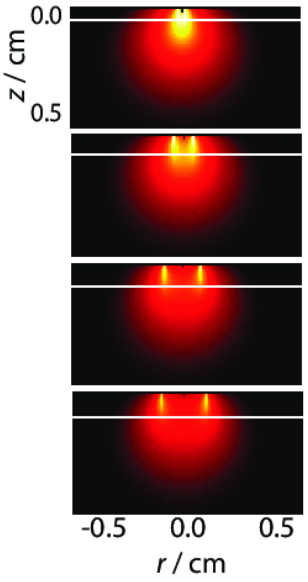

Figure 3.11: Penetration depth for four different fibre distances. From 400 µm (left) to 1 mm, 2 mm and 2.5 mm (right) for 1100 nm photons.

Because of the large amount of photons during a measurement, a statistical most-probable photon path can be estimated. The maximum depth of this path can be defined as the penetration depth [39]. Figure 3.11 shows MC simulations for how the penetration depth differs for fibre distances 400 µm, 1 mm, 2 mm and 2.5 mm at 1100 nm. The white line indicates the penetration depth for these photons. Table 1 presents that a greater fibre distance will give a deeper light penetration.

Table 1: Monte Carlo depth simulations

Fibre separation	400 µm	1 mm	2 mm	2.5 mm
Depth (cm)	0.06	0.10	0.12	0.13

The statistical maximum for photons for the four different fibre separations at 1100 nm.

4

INSTRUMENTS AND SOFTWARE

The instruments used in this project together with the developed software is presented in the following chapter. A description of the spectrometers and probes is presented together with a test of the system. Furthermore, the interface, signal processing and curve fit algorithms are described.

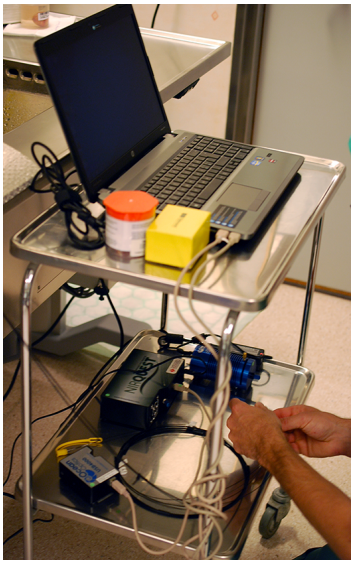

Figure 4.2: Instrumentation set up during a measurement.

4.1 OPTICAL SYSTEM

The setup consists of two miniature spectrometers, a light source, a probe and a computer, see Figure 4.1. The spectrometers are interconnected with the light source and the probe through optical fibres. The light source is a Tungsten-Halogen light source with an integrated shutter (Ocean Optics, HL-2000-FHSA). A visible range spectrometer (Ocean Optics, USB-4000-VIS-NIR) and a near infrared (Ocean Optics, NIRQuest-512) are used.

The system is portable, easily moved and can be packed down in two suitcases. One suitcase is for the computer and one is for the optical system. When brought to a measurement it can fit on a small surface, see Figure 4.2.

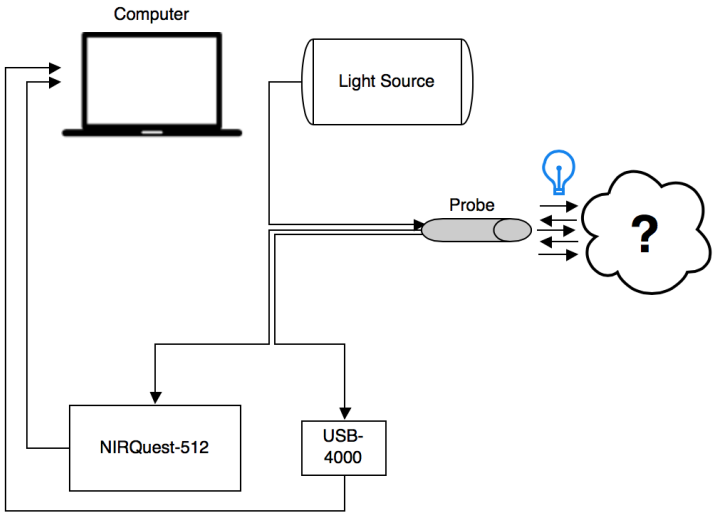

Figure 4.1: Setup for light source, spectrometers, probe and computer.

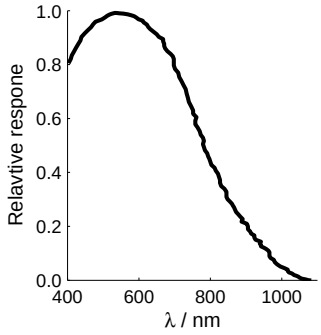

Figure 4.3: Relative response as a function of wavelength (λ) for Toshiba TCD1304AP. (Data extracted from "Toshiba TDC130AP" data sheet)

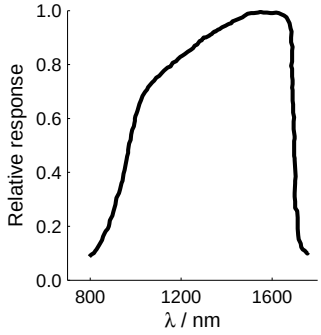

Figure 4.4: Relative response as a function of wavelength (λ) for Hamamatsu G9204-512 InGaAs. (Data extracted from "InGaAs linear image sensor G9301 to G9204" data sheet)

Spectrometer description

The USB-4000 has a 100 µm slit providing approximately a 4 nm optical resolution and a bandwidth of 349 - 1041 nm [40]. The NIRQuest-512 has a 25 µm slit providing approximately a 3 nm optical resolution with a bandwidth of 900 - 1700 nm [41]. Using both spectrometers, a spectrum is obtained in the the wavelength range 360 - 1700 nm. The USB-4000 has a Toshiba TCD1304AP linear CCD array detector and the NIRQuest-512 a Hamamatsu G9204-512 InGaAs linear array. The wavelength range is slightly reduced to 450 - 1600 nm due to the low sensitivity outside this range, see Figure 4.3 and Figure 4.4.

The detectors are influenced by noise which are categorised into three different kinds. Two of them, readout noise and dark noise, are caused by the instruments and can be regulated to some extent. Readout noise is present in any electrical circuitry. In this case, it is primarily caused by the generated voltage signal from the detector array and from the analog to digital conversion. Dark noise is caused by generation of electrons in the detector array through a thermal process. The dark noise is hence immensely dependent on the temperature of the device.

The third kind of noise, photoelectron noise, is noise in the detected light itself, and thus cannot be eliminated [42]. The signal-to-noise ratio (SNR) can though be manipulated as it depends on the number of photons detected, the more photons, the better signal-to-noise ratio.

Comparing the spectrometers

A comparison of the detectors SNR, noise level and pixel size can be viewed in Table 2.

Table 2: Detector specifications

	Toshiba	Hamamatsu	
SNR @ full signal	300:1	13000:1	-
Noise	45 (@ 50 ms)	15 (@ 1500 ms)	RMS counts/pixel
Pixel size	8 x 200	25 x 500	µm

SNR and noise specifications for the USB-4000 and NIRQuest-512. The USB-400 spectrometer is run at ambient room temperature, while the NIRQuest-512 spectrometer run with a cooled detector array. The two noise specifications are given for a single array read-out.

The USB-4000 achieves full signal with an integration time which is up to 100 times shorter than the NIRQuest-512, for a similar number of detected photons. We understand that this difference is mainly caused by different settings of the analog-to-digital conversion, i.e. the number of electrons per count. The longer integration time for the NIRQuest-512 with a higher number of photons detected provides a higher signal-to-noise ratio per readout (defined by the photoelectron noise as discussed briefly above). Because of this, a single acquisition from both spectrometers will result in the USB-4000 having more stochastic noise in the signal.

By signal averaging, the SNR for the USB-4000 would increase to 3000:1 by using 100 acquisitions, as the SNR increases by the square root of the number of samples [40]. Hence, the USB-400 would receive an equal integration time as the NIRQuest-512. This has not been used in this thesis because of longer computation times and slower real-time capture. Instead, post-processing of the signal has been implemented.

The dark noise and read out noise counts are unknown for the detectors. However, the NIRQuest-512 has a thermo-electric cooler (TEC) which helps it to reduce the noise by controlling its operating temperature. Hence, its dark noise count is reduced. The pixel size of the Hamamatsu detector is approximately eight times larger than the pixel size of the Toshiba [40, 43]. This, combined with the difference in integration times, results in the Hamamatsu detector receiving up to 800 times more photons per pixel, given the same photon flux. This fact in combination with the achieved signal-to-noise characteristics yields that the material sensitivity of the Hamamatsu detector is expected to be considerable lower than the one for the Toshiba detector.

The spectral response of the two spectrometers have peak values at 550 nm and 1550 nm respectively, in the range of interest. The relative sensitivity for the detectors is noticeably low in the range $800 < \lambda < 1000$ nm, especially for the USB-4000, see Figure 4.3 and Figure 4.4, which will also result in a higher stochastic noise in this region.

Probes

The optical probes used in biomedical applications consists of several optical fibers aligned in different formations, depending on application and chosen design. For diffuse reflection probes, a single illumination fibre with different numbers of spatially distributed collecting fibres are commonly used. [44]. For these applications fi-

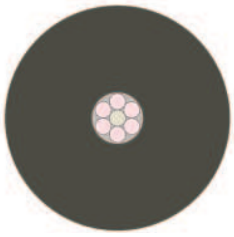

Figure 4.5: Probe 1 with one illuminating fibre and six collecting fibres.

Figure 4.6: Probe 2 with three fibres for possible source-detector separations 1 mm and 2 mm.

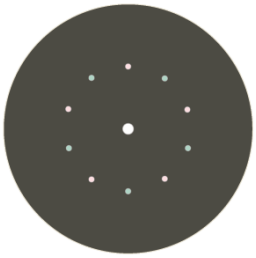

Figure 4.7: Probe 3 with fibre distance 2.5 mm. One illuminating fibre and ten collecting fibres.

bres with core diameters between 50 to 600 µm are usually used together with a doped cladding and a protective layer around it. The refractive indices of the core and the cladding define the numerical aperture (NA) of the fibre. The probe specifications in this project can be viewed in Table 3. Two probes have been tested and a third probe has been designed for future purposes:

- Probe 1 (Avantes, Reflection Probe (Standard)):
  The geometry of the probe head can be seen in Figure 4.5 with its six collecting fibre in a circular design and a single illuminating fibre core. The common part of the probe is enclosed in a stainless steel cover.
- Probe 2 (Custom made probe):
  The fibres are placed in a row of three fibres, see Figure 4.6. The fibres in this probe are not enclosed in a protective tube and are instead bundled up. In this project, this probe has been used during a majority of the measurements.
- Probe 3 (Trifurcated concentric fiber probe - Not tested):
  A circular design similar to Probe 1, however with a greater fibre distance, see Figure 4.7. The common part of the probe is enclosed in a black PVC-monocoil tubing whereas the legs are enclosed in black PVC furcation tubes.

Table 3: Probe specifications

	Probe 1	Probe 2	Probe 3	
Fibre separation (ρ)	0.4	1.0 / 2.0	2.5	[mm]
Core diameter (illuminating)	400	400	400	[µm]
Core diameter (collecting)	400	400	200	[µm]
Probe length	2.0	-	4.5	[m]
Common length	1.0	-	4.0	[m]
Leg length	1.0	-	0.5	[m]
NA	0.22	0.22	0.22	[-]
Size of ferrule	10	15	10	[mm]

Probe specification overview for the three different probes.

The fibre geometry of Probe 2 enabled the usage of different fibre distances. It was used either with the light source in the centre slot and the two spectrometers in the outer ones (ρ = 1 mm), or with the light source in one of the outer slots (ρ = 2 mm). When

using the 2 mm configuration of Probe 2 a fibre splitter was used (Avantes, Bifurcated fiber cable, FCB-IR200-2), to measure in the entire wavelength range simultaneously.

Design Probe 3

When probe 3 was designed, some important specifications were discussed:

- Penetration depth and probing volume
- SNR ratio
- Sterilisation
- Length of probe
- Fibre geometry

The custom made probe was designed to get an optimal fibre separation. The fibre separation was decided to be 2.5 mm, which enables a good depth penetration without compromising the SNR ratio [45]. The separation is also sufficient to support diffusion theory [44].

The positioning of the fibres over the slit in the spectrometers were designed to be optimised. Both slits are 1 mm high, therefore the five 200 µm fibres are positioned in a vertical alignment and the user will have to adjust this connection between probe and spectrometers manually, to ensure no signal is lost.

A circular fibre geometry was selected for the probe head to get a good signal, not altered by inhomogeneous tissue [11]. The probe will be used during surgery and should therefore be of sufficient length to not interfere with the regular operating procedures. The whole probe is encapsulated in metal to enable a complete sterilisation in an autoclave before surgery.

4.2 TEST OF SYSTEM

The white light source was tested through continuously acquiring reference spectrum from the moment it was turned on, and every 15 seconds for ten minutes. The same was made for the spectrometers by measuring the background spectrum, i.e. the noise, instead.

Both the light source and the spectrometers showed a quick response to stabilise after initialising the system. The light source showed no difference in the spectrum past 15 seconds after being switched on, seen in Figure 4.8.

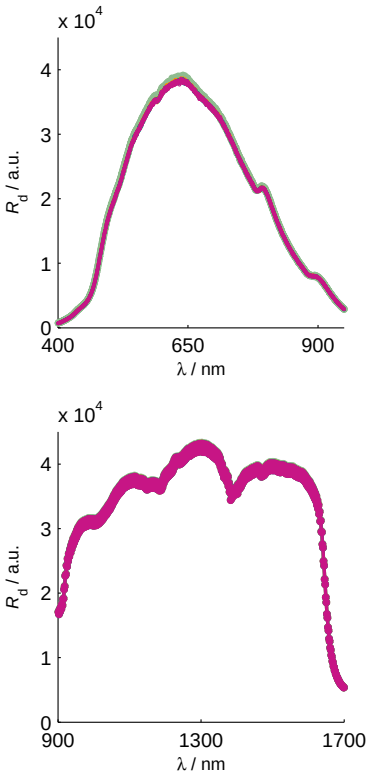

Figure 4.8: Diffuse reflectance (R_d) as a function of wavelength (λ) for investigation of light source stability. The diffuse reflectance the second the light was turned on (green) , after 15 s (pink/purple) and 1 min (orange).

The NIRQuest-512 can operate without its cooling fan, which was also tested. The most noticeable change was before and after the cooling fan was activated, seen in Figure 4.9. Afterwards, both spectrometers showed similar stability as the light source and were stable after 15 s.

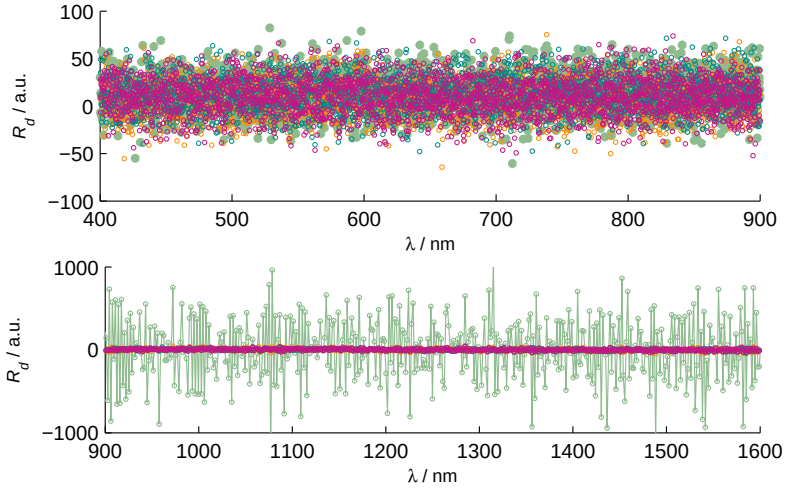

Figure 4.9: Diffuse reflectance (R_d) as a function of wavelength (λ) for investigation of the spectrometers background noise. The noise before cooling (green), at 1 s after turning on cooling (orange) and after 15 s (purple/pink). After 15 s the spectrometers were stable.

4.3 INTERFACE

A MATLAB program was developed with an assisting interface to automate the handling of data acquisition and analysis. The interface was designed to require minimum training to operate. The program is supposed to be operated by a nurse, or other personnel, as an operation takes place. It is, in such case, crucial that the program can be used with ease and hence a minimalistic design of the interface was desired.

A two window approach was designed. The design split up the coexisting functions into two windows, one named *spectrum_part*, which focuses on the real-time data, i.e on the actual measurements. While the other window, named *curve_part*, was solely to perform the curve fit and hence extract chromophore data from the measurements. Figures of the interface can be viewed in Appendix A. Both of the program windows included the ability to manage the data,

as it is essential that the first program can save data and the other load it.

Spectrum_part - in detail

A flow chart of the program is shown in Figure 4.10. The program initialises with running a few commands related to the spectrometers, as the spectrometers are found and a connection is set up. When started, the program is meant to be operated in the following way:

1. Select a suitable integration time. A choice of three different times can be selected.
2. Update the reference signal. The reference is measured by illuminating a reflective surface, a Spectralon reflectance standard (SRS-99-010, Labsphere, Inc., North Sutton, NH), and measure the diffuse reflectance to achieve a signal with high intensity, without saturating the detector.
3. Update the background by closing the shutter on the light source and measure the background noise.

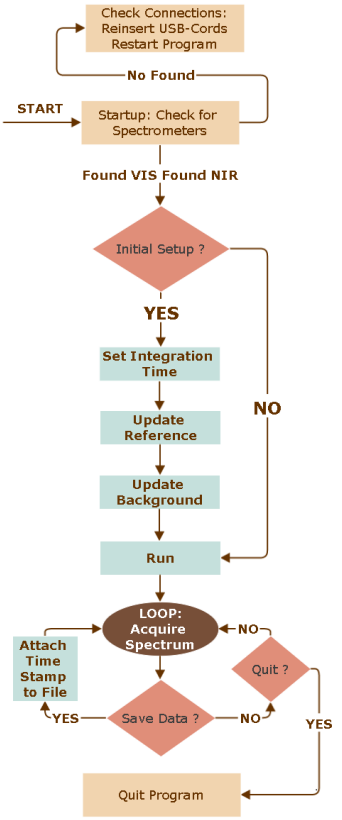

Figure 4.10: Flowchart of program spectrum_part.

The reference should resemble the one in Figure 4.11, where the count should come close to $6 \cdot 10^4$ (saturation limit for the detectors) for optimal sensitivity. These three presented steps are recommended to do on every startup of the program.

The acquired reflectance signal is calculated through

$$R_d(\lambda) = \frac{I_S(\lambda) - I_{Bg}(\lambda)}{I_{Ref}(\lambda) - I_{Bg}(\lambda)}, \tag{21}$$

where $I_S(\lambda)$ is the measured diffuse reflectance signal, $I_{Bg}(\lambda)$ the background noise and $I_{Ref}(\lambda)$ the reference signal. The diffused reflectance is thereby normalised in each instance of use since the raw signal is divided with the reference.

As mentioned, low sensitivity results in a low signal. In Equation 21, the denominator approaches zero in the regions where the reference signal is low, which results in random fluctuation in the acquired signal, also seen as noise.

Every time one of the functions (integration, reference, background) are performed, a *.mat*-file is saved. If the files are in the same or parent directory, it is possible to skip the updating of these files and use old values (*e.g* in case of unexpected program termination).

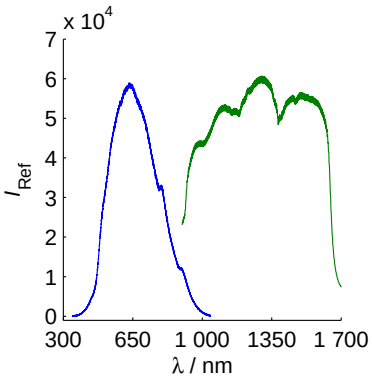

Figure 4.11: Intensity and shape of reference signal (I_{Ref}) as a function of wavelength (λ) for the reference spectra for the two spectrometers.

After the initial steps, the program is ready to run. A signal is continuously updated and displayed in the graph according to Equation 21. The spectrometers perform measurements with different efficiencies. The USB-4000 contains a lot more stochastic noise than the NIRQuest-512, despite the background reduction. However, it requires a very short integration time compared to the NIRQuest-512. To compensate for the stochastic noise, the visible signal is acquired five consecutive times and its average computed.

When using the program, the user can save spectra and choose the name of the saved files through the input field, however a name is not necessary. The files are saved in the same directory as the program is running from, with a time stamp attached to its name.

The data is saved as a *-struct* in *.mat*-files, containing:

- Wavelengths (λ)
- Raw signal ($I_S(\lambda)$)
- Diffuse reflectance ($R_d(\lambda)$)
- String with integration times

Curve_part - in detail

The curve fit window is used for data analysis. Saved files can be loaded and the program will connect the two spectra and perform some signal processing before displaying it in the window. After loading files the curve fit can be applied on a selected spectrum. If the chromophores add up to a percentage different from 100 % the user can chose to normalise the data to get a better overview of the chromophore composition. The normalised spectrum should not be taken as the unique solution but as a guideline to the real volume fractions.

4.4 SIGNAL PROCESSING

After a spectrum is acquired, the signal will be processed in several steps. The signal from the USB-4000 is considerably influenced by noise, hence the acquired signal is binned and filtered in MATLAB. A Savitzky-Golay filter is used since this filter is optimal to use for signals whose frequency span without noise is large. The filter minimises the least-square error when fitting a polynomial to a decided frame [46]. Different frame sizes and polynomials were tested and ultimately a frame size of 51 pixels and a first order polynomial was decided upon, which eliminated most of the noise and gave a good

Table 4: Parameter restrictions

	Lower boundary	Upper boundary	
Chromophores	0	100	[%]
a	100	10000	[m^{-1}]
b	0	10	[-]
f_{Ray}	0	1	[-]
R_v	0	0.1	[m]
k	0	1.5	[-]

The restrictions on the parameters incorporated in the model.

signal. After filtering the USB-4000 signal, binning of the signal is performed a second time.

When the USB-4000 signal has been processed, the two spectra are put together through a third order polynomial fit in the range 900 - 950 nm. If there is an offset between the two spectra the part from the NIRQuest-512 if multiplied by a factor to level it out. This factor is in most cases approximately one if the probe has been handled correct. Before the total spectrum is ready for analysis one final binning is performed to make the edges for the overlapping range smoother.

4.5 CURVE FIT

To analyse a gathered spectrum a Levenberg-Marquardt least-square algorithm is used in MATLAB, which previously have been used by other groups [30, 47]. The input to the algorithm is the solution to Equation 19 or Equation 20 with different combinations of the diffusion and scattering coefficients (Equation 4 or Equation 5). Appropriate restrictions are made on the parameters in the model, see Table 4.

For the curve fit to be as accurate as possible the volume fraction of the chromophores should add up to 100 %. To increase the stability of the fit, this can be implemented as an additional constraint, which have been suggested [28]. However, some deviations from this will be tolerated in this thesis, since there is always some uncertainty in the measurements.

5

METHODS AND VALIDATION

The validation was performed through phantom measurements, MC simulations and a TOFS measurement. In the following chapter the methods for the validation measurements are presented as well as their results. The results were analysed by adopting the scattering coefficient described by Equation 5, the light source modeled by Equation 19 and the diffusion coefficient, $D = [3\mu_s']^{-1}$. Further, unless else specified, the data is evaluated with Probe 2 and the fibre distance 2 mm.

5.1 TRANSMISSION MEASUREMENTS

Measurements were performed to extract the absorption coefficients for sunflower oil and pig lard, used as lipids in the phantoms. These were conducted by using a collimated transmission setup and a spectrophotometer. Reference measurements were performed on water since it has a known spectrum.

To measure the absorption of lard it had to be melted. Some irregularities due to different temperatures might be present as the lard was heated up and then cooled repeatedly.

Collimated transmission

Collimated transmission measurements were performed with the light source and the two spectrometers described in Chapter 4. The instruments were coupled to a cuvette holder (Thor Labs, CVH100) in which cuvettes containing the lipids were placed. Measurements of the transmitted light were performed in the wavelength range 400 - 1600 nm. Integration times of 30 ms for the USB-4000 and 2 s for the NIRQuest-512 were used. The USB-4000 acquired five consecutive spectra which were accumulated while it was sufficient with a single spectra for the NIRQuest-512. The absorption coefficient was calculated through the Beer-Lambert law, Equation 10, and compared to the known chromophore absorption spectra in Figure 3.2.

Spectrophotometer

The measurements were performed in the region 400 - 1100 nm. The spectrophotometer (Unicam, Helios Alpha, UV-Vis spectrophotometer) gave results in the dimensionless parameter absorbance. An integration time of 1 s was used with a single acquired measurement for each wavelength. Initially, a sweep was made over the entire region and a general spectrum was obtained. Afterwards, the measurement points were taken in intervals of 10 nm for regions with high absorbance since the instrument could not resolve points with low absorbance.

Results

The measurements of the absorption coefficients for sunflower oil, pig lard and water followed the expected spectra quite accurately in the NIR range. However, there was a slight offset due to problems with finding a suitable reference. For the visible region the spectrophotometer and the collimated transmission setup were not sufficiently sensitive to detect the weak absorption of the oil. For the collimated transmission, the calculated absorption coefficient in the range 400 - 900 nm was larger than tabulated values found in references [48, 49], probably due to scattering in the region. The spectrophotometer was only able to resolve the visible wavelengths between 400 - 500 nm; in this region the lipid absorption is stronger. The lower limit of resolution for the spectrophotometer is estimated to be $\mu_a = 0.1\ \mathrm{cm}^{-1}$.

5.2 PHANTOMS

A phantom study was completed to validate the instruments and the presented diffusion model. Phantoms are virtual tissues that can take different forms, both liquid and solid. The advantage of phantoms are that one can control the magnitude of the optical properties by mixing different ingredients in different proportions. The created phantoms were both liquid and gel-like. These were mixed with different fractions of a water based solution (PBS), blood and different lipids. Blood was the absorber in the phantom and the lipids the scattering component. Measurements were conducted on approximately 100 phantoms. There is no gold standard for phantoms, so an appropriate way to mix the phantoms needed to be found. In the following evaluation, the expected absorption coefficients are based on spectra in Figure 3.2.

Choosing the lipids

Lipids and water are difficult to mix since they repel each other, therefore different techniques were tested to mix the two. The lipids in the phantoms were either intralipid, sunflower oil or pig lard. There was no problem mixing phantoms with intralipid since it is emulsified and has known optical properties. However, intralipid cannot provide high enough fractions of lipid to the phantoms [50, 51]. Different phantom recipes have been suggested in the literature, one way to mix water and lipid is to use agar as an emulsifier. Phantoms with agar have previously been mixed with as much as 50 % lipids [52]. Another suggested recipe is to mix water and lipid with Triton X-100. Using Triton-X100 has proved successful for up to a 70 % lipid fraction [30, 52, 53, 54].

INTRALIPID PHANTOMS

The intralipid phantoms were mixed on a magnetic stirrer and heated to 37^{o}C one hour prior to the experiment for the phantom to be homogeneous and the temperature stable. A first set of phantoms were prepared with water, blood and intralipid, see Figure 5.1. The measurements were performed with two different source-detector separations (1 and 2 mm) using Probe 2. The phantoms were prepared with blood volume fractions varying between 1 % and 10 % in eight phantoms and the fraction of intralipid varying between 1 % and 5 % in five phantoms, since this seems to be common percentages to use [55].

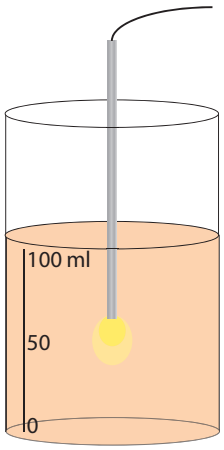

Figure 5.1: Schematic picture of measurement in an intralipid phantoms.

A second set of phantoms were also prepared with the same recipe to see if the results were reproducible. For the second set the measurements were only acquired with the 2 mm distance. In the second set a greater range of intralipid volumes were also investigated. The volumes were 3, 6, 9, 15, 20 and 25 %. All were tested for blood volume fractions between 1 - 10 % as previously. During the second set, some of the measurements were acquired two times in the same phantoms. Both with the magnetic stirrer on and with it off, too see if the stirring would affect the results.

Results

Acquired spectra for phantoms with varying intralipid and blood volumes are shown in Figure 5.2. An increase of blood resulted in a lower signal and an increase of intralipid a stronger signal.

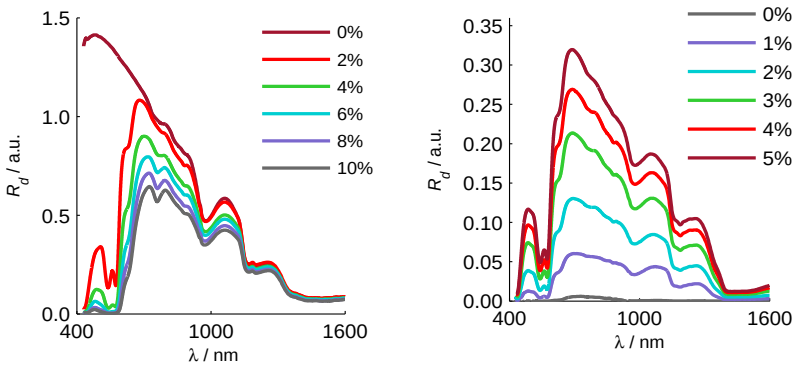

(a) Increasing blood (b) Increasing intralipid

Figure 5.2: Diffuse reflectance (R_d) as a function of wavelength (λ). Trend of spectra for (a) increasing blood and (b) increasing intralipid in the phantoms.

The general trend in the results are that the blood volume fractions are underestimated. The underestimation is 0 - 3 % percentage points for intralipid levels between 0 - 10 %, which gives an average relative error of 30 - 50 %. The model greatly overestimated the blood absorption for fractions of intralipid greater than 10 %. The estimated blood volume as a function of the expected blood volume are shown in Figure 5.3.

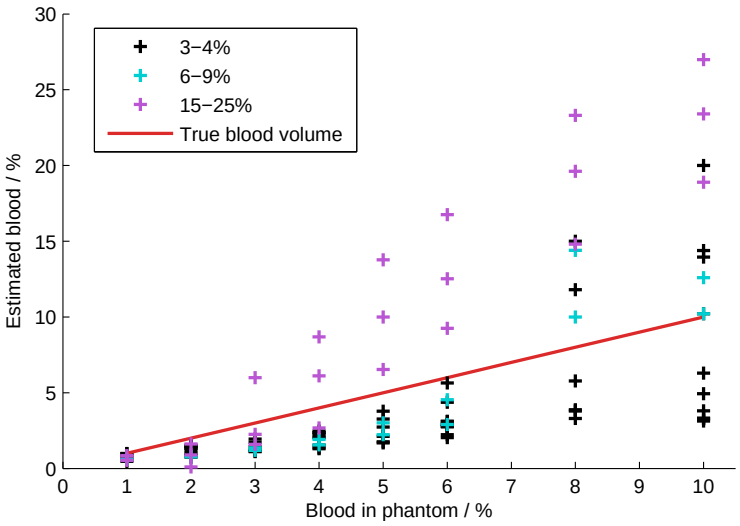

Figure 5.3: Estimated blood volume fraction as a function of the expected blood volume (red) for blood fractions from 1 - 10 %. Intralipid fractions were 3 - 4 % (black), 6 - 9 % (blue) and 15 - 25 % (purple).

The errors for the estimated blood volume were systematic and could be compensated for by finding a linear regression based on the acquired data. The first order polynomials were calculated to $y = 0.45x + 0.3$, for 3 - 4 % intralipid and $y = 2.3x - 3$, for 15 - 25 % intralipid. The compensated spectra are shown in Figure 5.4.

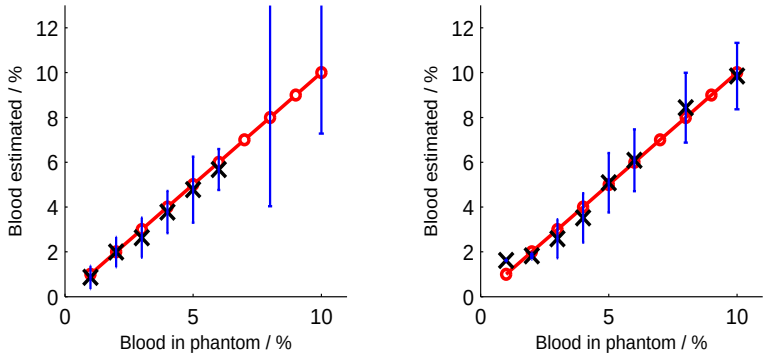

(a) 3-4% intralipid (b) 15-25% intralipid

Figure 5.4: Systematically corrected blood volume estimations (blue) as a function of the expected blood volume (red) using (a) 3 - 4 % intralipid (b) 15 - 25 % intralipid. In (a) the 8 and 10 % blood volumes were greatly overestimated and their average is not visible.

Analysis of the curve fit was performed by studying the behaviour of the residual. The general features was an increased level of intralipid, from 1 - 5 %, resulted in a smaller residual and a larger blood volume increased the residual.

See Figure 5.5 for a typical curve fit and Figure 5.6 for the residual of varying intralipid. Generally, the curve fit works well up to 900 nm and after 900 nm it deviates depending of the absorption and scattering properties.

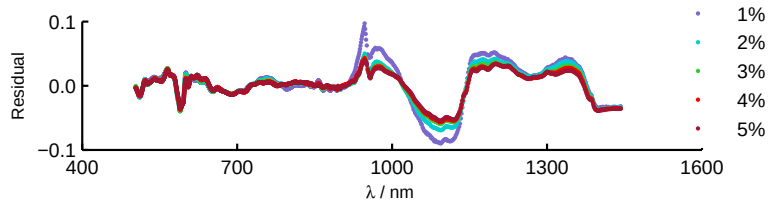

Figure 5.6: Residual as a function of wavelength (λ) for measurements with varying intralipid.

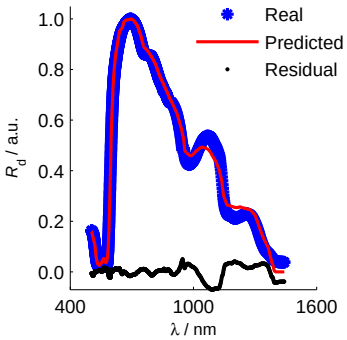

Figure 5.5: Normalised diffuse reflectance (R_d) as a function of wavelength (λ). Result of a curve fit, as shown the deviations are for wavelengths greater than 900 nm.

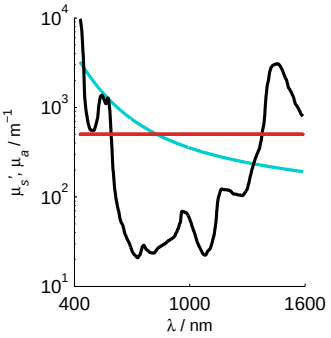

Figure 5.7: Reduced scattering (blue), absorption (black) and reciprocal fibre separation (red) as a function of wavelength (λ) for a phantom containing 5 % blood and 3 % intralipid.

Since the reduced scattering coefficient was a free parameter in the curve fit, it was also studied. Equation 5 was used to model the reduced scattering coefficient and when the intralipid fraction was increased the outcome was an increase of a and f_{Ray}, and a decrease of b. The same trends were further noticed for increasing fractions of blood in the phantoms, but not on the same scale as when increasing the intralipid volume.

Figure 5.7 shows a comparison of the absorption and reduced scattering coefficient for a phantom with 5 % blood and 3 % intralipid. One can clearly see that the two diffusion criteria, $\mu_s' >> \mu_a$ and $\mu_s' > 1/\rho$, are not fulfilled in the majority of the region.

Another element to consider is that the curve fit usually calculates the water volume fraction to 100 %. The model restricts it from finding a higher value since the parameters in the curve fit have an upper boundary as stated in Table 4.

Lastly, measurements were performed in the phantoms both still and while stirred with the magnetic stirrer. No difference could be seen either in the curve fit or in plots of the two cases.

AGAR PHANTOMS

The second phantoms used agar as emulsifier to mix in a greater fraction of lipids. In the agar phantoms sunflower oil was used as the lipid component. The absorption of sunflower oil has been measured previously but does not mimic tissue well for all wavelengths [48].

The agar was heated to 90$^{\text{o}}$C together with water on the magnetic stirrer. The amount of agar added to the phantom was 1 % of the total water volume. The heated mixture was together with sunflower oil and blood poured in 4 ml containers and shaken while cooling down. As the phantoms were getting cooler the liquid became a gel-like substance. The same phantoms were produced 3 - 5 times to show reproducibility. During the measurement the probe was held fixed inside the phantom.

Results

Mixing the agar phantoms was not trivial. During the process small air bubbles entered the solution and this caused the phantoms to be highly scattering. Furthermore, it was hard to confirm that the phantoms were homogeneous due to these bubbles.

Since no absorption spectra of sunflower oil was obtained during the transmission measurements, no evaluation of the lipid content

was made. The expected blood volume fractions varied from 2.7 % to 3.5 %. When running the curve fit, with lipid excluded, blood volume fractions between 1.5 - 3.1 % were found. This underestimation of blood is more satisfying than for the intralipid phantoms with the average percentage point error being 0.88 % and the average relative error 29 %. Figure 5.8 shows the estimated blood volume fractions compared to the expected blood volume fractions for the agar phantoms.

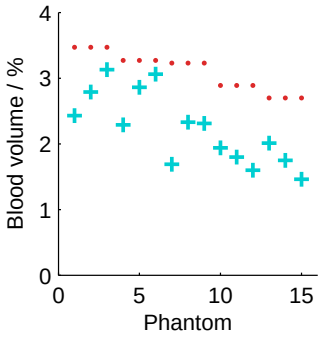

Figure 5.8: Expected (red) and estimated (blue) blood volumes for the agar phantoms without lipid in the curve fit.

TRITON-X100 PHANTOMS

The third set of phantoms used were water, blood and lipids emulsified with Triton-X. The quantity of Triton-X was about 1 - 2 % of the total volume of lipids. The lipid used in the Triton-X phantoms was pig lard which has an absorption spectra similar to that of lipids in the human body [49]. The lard was melted on the magnetic stirrer and when it was a clear liquid, Triton-X was added and the two components were mixed for about 15 minutes at 60^{o}C. The mixture was kept at the same temperature while water, blood and intralipid were gradually mixed in. Measurements were performed with lipid volume fractions of 5, 10, 15, 20 and 25 % and while stirring the phantoms, to keep them as homogeneous as possible.

Results

The Triton-X100 gave varying results. Yet again, there were some problems mixing the phantoms homogeneously, due to the large particle size of lard. In general, the model overestimated the lipid volume fraction with as much as 15 - 20 %. However, the algorithm came closer to the expected value for blood. The average percentage point error was 1.06 % while the relative error was 27 % for blood, see Figure 5.9.

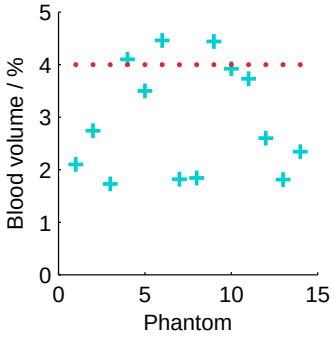

Figure 5.9: Expected (red) and estimated (blue) blood volumes for the Triton-X100 phantoms with lipid in the curve fit.

5.3 MONTE CARLO

MC simulations were used to further validate the instruments and the model. MC simulations are considered the gold standard for tissue optics, since MC does not depend on any approximations. It is thus not dependent on the reduced scattering being greater than the absorption. The MC algorithm used was Monte Carlo for Multi-Layered media (MCML) for steady state light transport and is described in reference [56].

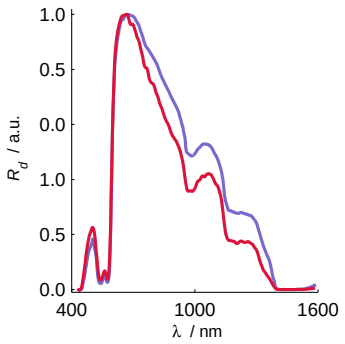

Figure 5.10: Diffuse reflectance (R_d) as a function of wavelength (λ) for MC simulation (blue) and diffusion model (red) for a phantom containing 3 % intralipid, 3 % blood and 94 % water.

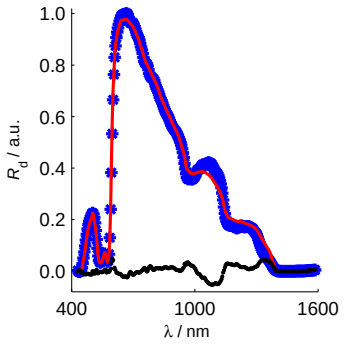

Figure 5.11: Diffuse reflectance (R_d) as a function of wavelength (λ) for MC simulation (blue) with the curve fit algorithm (red) and residual (black) for a phantom containing 3 % intralipid, 3 % blood and 94 % water.

MC simulations were carried out with experimentally extracted liver values of scattering and absorption [26] and the curve fit algorithm was tested on the output spectrum from the simulation. A similar validating simulation was performed with the optical properties of an intralipid based phantom to evaluate the performance of the curve fit and the usage of the diffusion approximation in this regime.

Results

The MC simulation was compared to the diffusion model for a virtual tissue, seen in Figure 5.10. The two methods agree up to 700 nm while they differ in the NIR region. The input values in the simulation was the expected data from a phantom (3 % intralipid, 3 % blood and 94 % water). Figure 5.11 shows the performance of the curve fit on the simulated data. The curve fit gave a better approximation for the MC simulation than in the phantom study. The new estimation of blood was 2.74 % compared to ∼1.5 % for the phantoms.

When comparing the MC simulation from a liver, seen in Figure 5.12, the diffusion model comes close to describing the propagation of light in the tissue, and performs more accurately than in the phantoms. When running the curve fit on the MC data the algorithm found a fit with a small residual, see Figure 5.13. The results from the curve fit are presented in Table 2.

Table 2: Monte Carlo Result

Average (%)	MC input	Curve fit
Water	76	74
Lipid	16	13
Blood	3.2	2.4
O_2 saturation	8.0	0.0
Bile	5.5	13
Scattering	MC input	Curve fit
μ_s' (800 nm)	1700	1600
Mie Slope	1.2	1.6
f_{Ray}	0.56	0.38

Input to MC simulation of liver from reference [26] and result from performing the implemented curve fit on the MC data.

The results from the curve fit are close to the true values used as input to the simulation. The model underestimates the chromophores water, blood and lipid, but is still within the standard deviation from the data in reference [26], and overestimated bile.

In Figure 5.14 the evaluated scattering coefficient is compared to the absorption coefficient and the reciprocal fibre separation for the simulated MC liver. Here, diffusion theory is valid in a greater region ($\lambda < 1400$ nm) than in Figure 5.7.

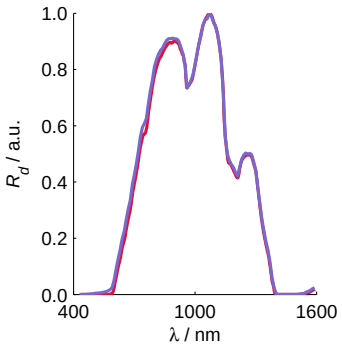

Figure 5.12: Diffuse reflectance (R_d) as a function of wavelength (λ) for MC simulation (blue) and diffusion model (red) for liver tissue. Input data is the first column in Table 2.

5.4 TIME-OF-FLIGHT SPECTROSCOPY

TOFS was used as a third way to validate the instruments and the optical properties of the phantoms. Information about the TOFS system can be found in reference [57]. The measurements were performed in three different wavelength ranges, 590 - 690, 960 - 1020 and 1080 - 1200 nm on four phantoms. The TOFS measurements were compared to the expected absorption and scattering coefficients and to the results from the curve fit to see if they agreed.

Results

Some of the measurements were hard to perform due to a low signal-to-noise ratio. The best signal came from the phantom containing 3 % intralipid and 3 % blood, which is presented while the others are excluded. The absorption values from TOFS came closer to the estimation of the curve fit than the expected values. The scattering TOFS overlapped both the expected and estimated values, see Figure 5.15.

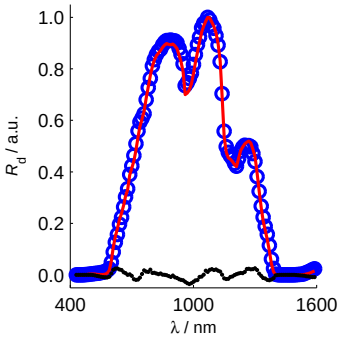

Figure 5.13: Diffuse reflectance (R_d) as a function of wavelength (λ) for MC simulation (blue) with the curve fit (red) and residual (black) for liver tissue.

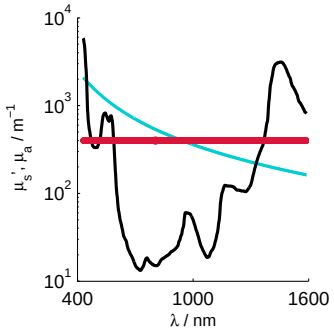

Figure 5.14: The scattering coefficient (blue), absorption coefficient (black) and reciprocal fibre separation (red) as a function of wavelength (λ) for the MC liver.

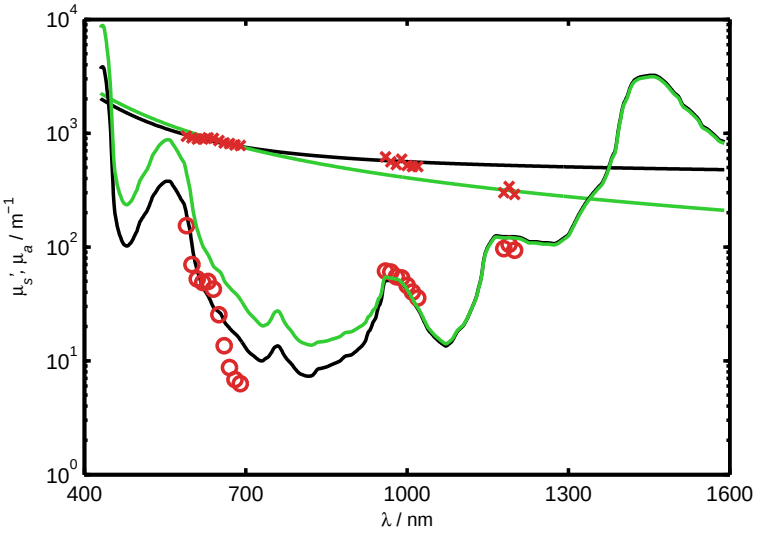

Figure 5.15: Scattering (μ_s') and absorption (μ_a) as a function of wavelength (λ) for TOFS (red), DRS (black) and expected values (green).

6 LIVER MEASUREMENTS

Opportunities arose to do *ex vivo* measurements on murinae organs, porcine liver and on human liver tissue recently resected during surgery at Lund University Hospital. Most of the liver measurements gave results with a strong correlation between signal and evaluated curve. The results were also similar compared to previous studies.

6.1 EX VIVO MURINAE ORGAN MEASUREMENTS

Measurements were performed on 13 - 14 organs in five different mice at the Biomedical Center at Lund University. The mice were part of a research project conducted by Oskar Vilhelmsson Timmermand. The murinae measurements were ethically approved through "Malmö/Lund djurförsöksetiska nämnd".

The mice were sacrificed, dissected and had their radioactivity and weight measured for each organ before the optical measurements could be performed. Probe 1 and Probe 2 (both fibre separations) were used for all measurements. The task was to try to identify the blood volume fraction in each of the organs. Between 7 - 8 diffuse reflectance measurements were performed on each organ summing up to between 90-110 measurements on each mouse.

Two to three measurements were acquired with each probe in different spots, which resulted in a total measurement time of 40 minutes for each mouse. The organs dried out rather quickly, thus affecting both the blood and water volume fraction for the measurements carried out towards the end. New reference and background spectra were acquired for each mouse and every time the probe was switched.

Analysis was only performed on the liver organs since they were of interest in this project.

Results

The results from the murinae livers were satisfying. In total 76 measurements were acquired and 69 were used for further analysis. The measurements that were not used either had an unsatisfactory curve fit or a different shape of the spectrum. One measurement

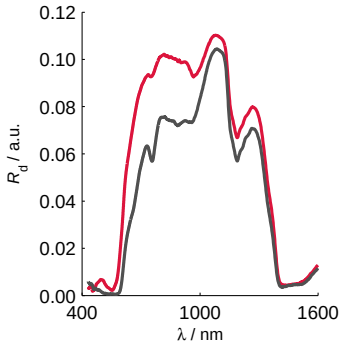

Figure 6.1: Diffuse reflectance (R_d) as a function of wavelength (λ) for the two distinct diffuse reflectance spectra from the murinae liver, measured with the 1 mm probe. The shape of the spectra for mouse 1 - 4 (red) were similar looking and mouse 5 (grey) had a different shape to it's spectra.

deviated more than 2 standard deviations (σ) from the mean and was also excluded.

Two fits were made for all organs, one including all chromophores and the pigment packing factor (Full fit) and one containing only water, lipids and blood, without pigment packing (WBF fit). Both fits gave similar results for the volume fractions of the chromophores.

The summation of all chromophores for Probe 1 and 2 can be viewed in Table 3. The WBF fit gave the best results for all probes, even though the result for the 2 mm distance is more or less the same.

The results showed two typical shapes of the diffuse reflectance. Mouse 1-4 had similar spectra when normalised and mouse 5 had a different shaped curve, see Figure 6.1. According to the curve fit mouse 5 had more blood in its liver compared to mouse 1 - 4.

Figure 6.2 shows an acquired murinae liver spectrum and its fit.

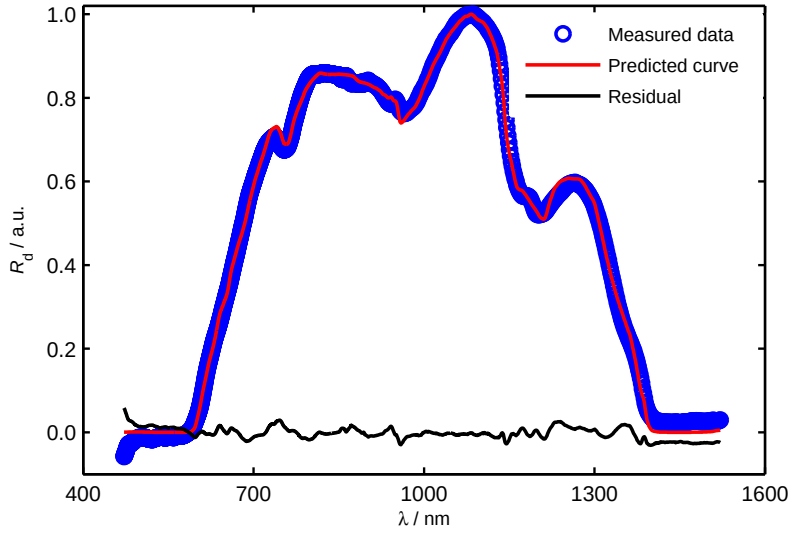

Figure 6.2: Normalised diffuse reflectance (R_d) as a function of wavelength (λ). Acquired signal and corresponding curve fit for a typical measurement for Mouse 2. The chromophores are calculated to 66 % water, 10 % blood, 20 % lipids and 2 % bile. The sum of all chromophores add up to 98 %.

6.2 EX VIVO PORCINE LIVER MEASUREMENTS

Ex vivo measurements were performed on a porcine liver as an attempt to test the curve fit algorithm and to compare the spectra for

Table 3: Murinae measurements

Average (%)	400 µm	1 mm	2 mm	2 mm*
Full fit	155 ± 26	131 ± 23	106 ± 12	103 ± 9
WBF fit	147 ± 24	126 ± 20	106 ± 14	102 ± 8

Average summation of chromophores by the curve fit for the two different fits and the three different probes. *measurements with a standard deviation $>2\sigma$ excluded.

the different source-detector separations. During the course of the project two livers were obtained. The first liver was kept for three days in a fridge and measurements were performed each day. The measurements from the first day were all with the 1 mm source-detector separation and with the probe being hand held. During the second day spectra were acquired with Probe 1 and Probe 2 with both fibre separations. Figure 6.3 shows a porcine liver during a measurement with Probe 1. The probe was also mounted on a stand for two sets of measurements and hand-held for one set to be able to compare the stability of the technique. The third day measurements were taken only with the 2 mm separation, and the integration time was manually set to four times greater than the reference.

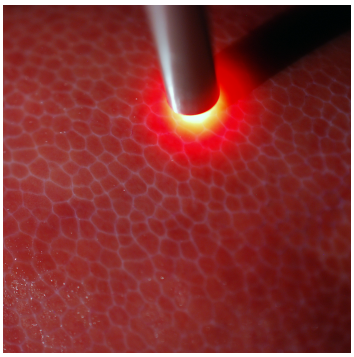

Figure 6.3: Surface of porcine liver together with Probe 1.

The second porcine liver was obtained towards the end of the project. Measurements were performed to further analyse the stability of the curve fit and the extraction of the chromophore volume fractions. The measurements were carried out during two days and about 20 measurement points were acquired each day to get better statistics.

Results

For the first porcine liver all spectra that were obtained during the first two days had similar shapes. No difference could be detected when the probe was touching and when the probe was inducing a pressure on the liver surface. The results from the third day cannot be used. When the integration time was increased by a factor of four, compared to the reference, analysis showed a non-linearity for the NIRQuest-512.

Measurements were acquired with the probe being hand held or held by a stand. As before, no major difference could be detected in the shape of the spectra. The integration time for this was quite short, 23 ms for the USB-4000 and 1.5 s for NIRQuest-512.

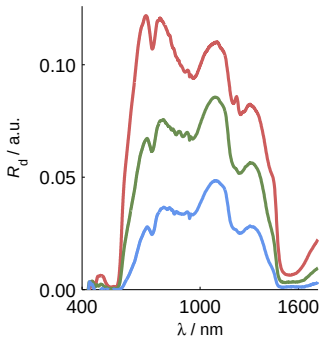

Figure 6.4: Diffuse reflectance (R_d) for porcine liver as a function of wavelength (λ) for different fibre separations, 400 µm (red), 1 mm (green) and 2 mm (blue). All spectra were acquired with the same integration time.

Different fibre separations are compared in Figure 6.4 and the shorter the distance, the higher the signal is achieved.

During the first day, measurements were performed with a fibre separation of 1 mm and the results from the curve fit were good and consistent. For 8 measuring points, the average total summation was 101.8 % with volume fractions calculated to 75.8 ± 6.8 % water, 8.9 ± 2.9 % blood and 17 ± 1.9 % lipid.

The second liver also showed consistent results. When comparing the results from the two days there was less liquid (water and blood) during the second day, which agrees with the fact that the liver should be more dehydrated, see Table 4.

Table 4: Porcine measurements

Average %	Day 1	Day 2
Total	112 ± 4	101 ± 4
Water	77 ± 4	66 ± 3
Lipid	26 ± 2	27 ± 2
Blood	10 ± 3	8 ± 2

Comparison between the two days for the second porcine liver.

6.3 EX VIVO HUMAN LIVER MEASUREMENTS

Figure 6.5: Measurement at Lund University hospital at a resected liver part.

Several *ex vivo* measurements on human liver were performed. The liver parts were resected from patients who had tumour metastasis in the liver and the measurements started within approximately 20 minutes of the extraction, see Figure 6.5. The sample was measured on during 30 - 40 minutes before being returned and sent to the pathologist. The last measurements were hence performed within one hour of the extraction.

The time used for each surgical procedure differed for each operation, but was typically well over three hours. During the time, the arteries and veins are gradually throttled in the part of liver which later was to be resected. The oxygenation within the sample was presumably close to none due to the time outside the body, but foremost the time required for the surgical procedure.

The measured points were selected over two rows on the liver surface with 5 - 6 points in each row. Several measurements were also acquired on the slightly lighter tissue, which would indicate a tumour or malignant tissue. To minimise the human error, each

point was measured twice whilst lifting the probe from the surface between the measurements.

The measurements were repeated with both Probe 1 and 2 during the measurements of the first and third patient. The sample of the second patient's liver was smaller and the time measuring the sample was limited due to the risk of dehydration. Hence, the second patient's liver was only measured with Probe 2.

Sterilisation

Measurements were performed with and without a sterile plastic cover, see Figure 6.6. The future of this project is aimed at performing measurements during surgery. This demands the probe and the instruments to pass certain requirements regarding sterile processing. Even with Probe 3, a plastic pouch will be required. To validate the use of such a pouch, the measurements were performed with and without a pouch to investigate its feasibility and how much it influenced the acquired data. The measurements performed with the plastic pouch are referred to as *coating*. The comparison is an approximate, since the different techniques were done independently. Hence, measurements were not acquired in the exact same spot.

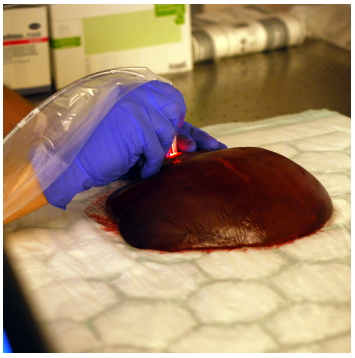

Figure 6.6: Measurement on a resected liver part using the plastic pouch with the probe.

Results

The measurements showed different results. Two out of the three patients gave good results for healthy tissue when comparing the data with previous studies [47], see Figure 6.7. The curves were also similar throughout the different measurement, as shown in Figure 6.8. The curve fit worked well on the different measurements, evaluating a curve with a small residual. The second liver was different both in the shape of the spectrum and in the calculated curve fit.

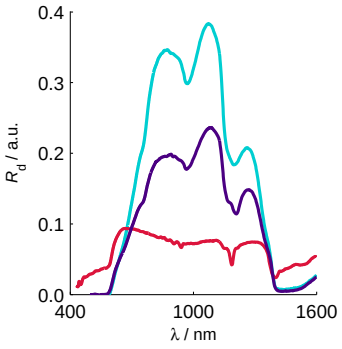

Figure 6.7: Diffuse reflectance (R_d) as a function of wavelength (λ) from three different liver patients. The red curve is from the second patient.

The use of the plastic pouch proved to have little effect on the acquired signal, see Figure 6.9. The shapes with and without the pouch are similar. Some deviations in intensity did occur but no reference was acquired with the pouch.

The average results for Probe 2 is presented in Table 5 for all three patients. The evaluation of the chromophores were similar in most cases, however, there were several measured points that deviated from average When the curve fit displayed a different result, the total summation was usually lower, but with a similar ratio for all chromophores. For two seemingly similar curves the chromophore content showed an expected value in one case and only half of the

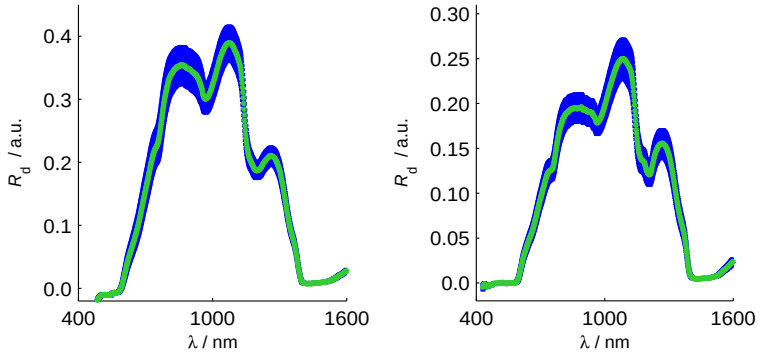

(a) Patient 1 (Probe 2) (b) Patient 3 (Probe 2)

Figure 6.8: Diffuse reflectance (R_d) as a function of wavelength (λ). Averaged spectra (green line) with corresponding standard deviation (blue bars) for (a) patient 1 and (b) patient 3.

volume in the other. A normal result of, e.g. 55 % water content was instead 25 %, and similar, bile was 15 % instead of 7 %. When the total summation was too low the scattering coefficient was greatly overestimated.

Table 5: Ex vivo human liver

Average %	1	2	3
Total	104 ± 3	67 ± 7	91 ± 17
Water	64 ± 3	22 ± 4	47 ± 10
Lipid	20 ± 1	40 ± 3	25 ± 5
Blood	6 ± 1	4 ± 1	5 ± 1
O_2 saturation	11 ± 11	100 ± 1	3 ± 4
Bile	15 ± 2	0 ± 0	13 ± 3

Average results for the healthy liver parts with Probe 2 for the three patients. The evaluation of chromophore data adding up to less than 50% for all chromophores together (6 measurements) have been excluded.

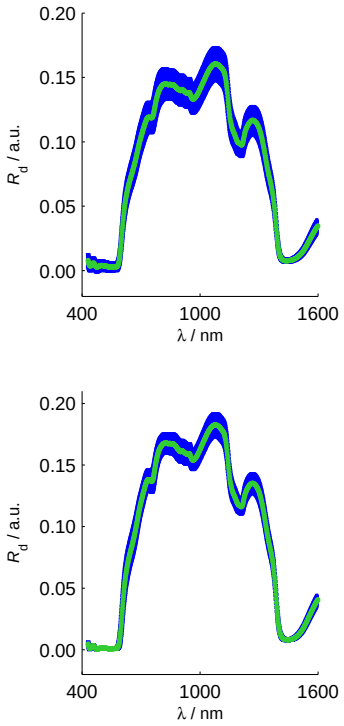

Figure 6.9: Diffuse reflectance (R_d) as a function of wavelength (λ). Statistical average of coating (top) and no coating (bottom) with the average (green) and standard deviation (blue).

Tumour tissue

The regions with tumours were fairly easy to distinguish with their lighter tissue colour. Their measured spectra also confirmed this, containing more diffuse reflected light for visible wavelengths. A comparison between normal tissue and tumour tissue is shown in

Figure 6.10. The malignant tissue showed a trend of increased water and a decrease of fat, blood and bile content. In the tumours the reduced scattering at 800 nm was lower compared to healthy tissue. The scattering power (Mie Slope) also decreased but varied more for the healthy tissue and hence conclusion could be drawn from this.

The second patients data differed significantly from the first and third, and no distinction between tumour and healthy tissue could be established on the sample. The average of healthy and malignant tissue chromophore composition and scattering properties for patients 1 and 3 are presented in Table 6. An explanation for the second patient is not yet established, and thus not included in the table.

Table 6: Ex vivo human liver

Average (%)	Healthy	Malignant
Total	100 ± 12	123 ± 12
Water	58 ± 11	91 ± 12
Lipid	22 ± 4	21 ± 4
Blood	6 ± 1	6 ± 2
O_2 saturation	8 ± 9	49 ± 35
Bile	14 ± 2	6 ± 7
Scattering	Healthy	Malignant
μ_s' (800 nm)	1790	1050
Mie slope	1.2	0.9

Averaged chromophore data, reduced scattering at 800 nm and calculated Mie slope, for patients 1 and 3.

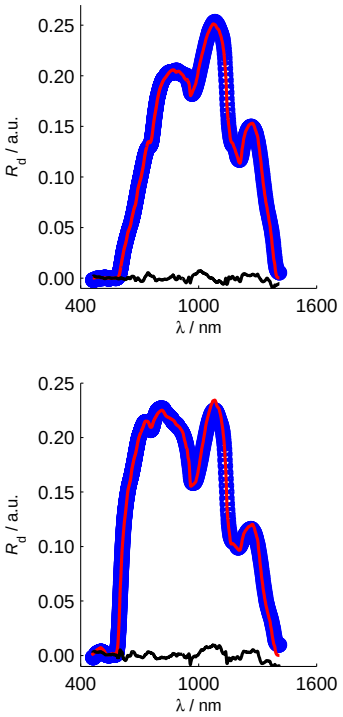

Figure 6.10: Diffuse reflectance (R_d) as a function of wavelength (λ). Acquired spectra (blue) with corresponding curve fits (red) and residual (black) for healthy tissue (top) and malignant tissue (bottom).

Fibre distance comparison

In Figure 6.11 the average summation for Probe 1 and Probe 2 are plotted with their standard deviation.

The 400 µm fibre separation does not work well with the model and the summation of the chromophores is above 200 % for most measurements; the standard deviation is also larger than tolerable. The separation of 2 mm both gives a total summation closer to 100 % and a more acceptable standard deviation.

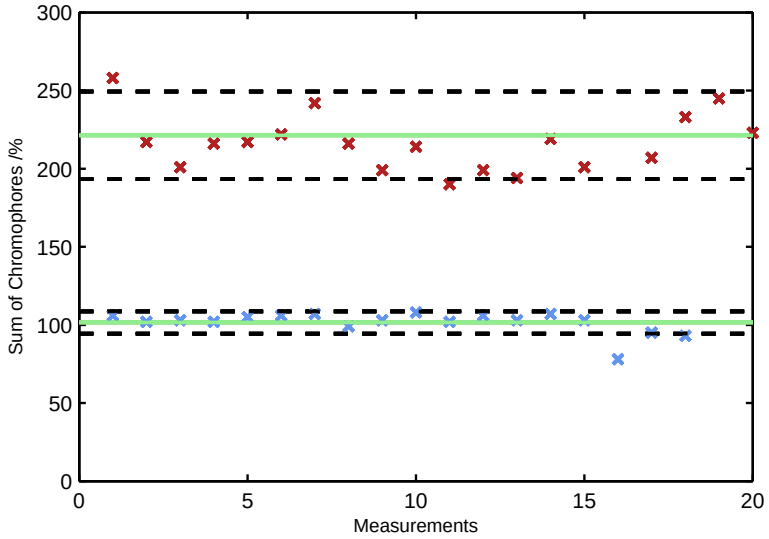

Figure 6.11: Summation of chromophore data with their average (solid line) and standard deviation (dashed line) for Probe 1 (red) and Probe 2 (blue).

7 DISCUSSION

In the following chapters discussions are made of the used approximations, the results and the curve fitting algorithm. In detail, the discussion will be of the phantom preparation and validation and of the liver measurements.

7.1 APPROXIMATIONS

Diffusion

For regions with high absorption, and when using a probe with a short fibre distance, diffusion was not a good approximation. For short fibre distances, measurements on tissue are more likely to be affected by inhomogeneous structures. This contributes to larger irregularities between measurements.

Probe 3 will hopefully give more accurate results with a 0.5 mm greater fibre separation than Probe 2. This probe will both meet the diffusion criteria in a more adequate way and will also probe a larger volume.

Temperature dependency

The shift in absorption spectra was assumed not to change for varying temperature. This approximation was sufficient for the phantoms containing intralipid together with blood and water since they were kept at a constant temperature [30]. For phantoms containing the emulsifiers agar and Triton-X100, heating and cooling down of the phantoms were performed in several steps. The Triton-X100 phantoms were also measured at 60^{o}C, which is very high compared to 20^{o}C or 37^{o}C. How greatly this affected the phantoms is unknown since the results were not adequate. However, the change in lipid temperature is more likely to influence the scattering properties of the phantoms.

7.2 RESULTS

Transmission

The transmission measurements did not give as good results as expected, due the spectrophotometers low sensitivity and limited dynamic range. The spectrophotometers detection range only went to 1100 nm, which was not sufficient to fully cover the range of interest. For this project a spectrophotometer up to 2000 nm would have been desirable.

In the collimated transmission setup there was a lot of noise in the visible region. This might be due to too much scattering, since scattering is more prominent in this region. Furthermore, it was hard to find an appropriate non-absorbing reference. For the transmission measurements, no suitable reference was used. These measurements were not of high significance for the project, since good tabulated data was available. The measurements were mainly to confirm if the lipid spectrum was similar to the one in Figure 3.2, which it was.

Phantoms

Some difficulties arose in controlling the optical properties of the phantoms. The curve fit kept underestimating the blood volume, possibly due to the diffusion approximation or the performance of the curve fit. If the diffusion criteria was not met the estimation should have been better for larger fractions of intralipid, but this was not the case. When using intralipid volume fractions between 10 - 25 %, the blood was overestimated. No explanation for this has been found.

When comparing the scattering with the absorption and the reciprocal fibre separation, it indicates that the diffusion model is invalid in a majority of the wavelength range. However, the TOFS measurements came closer to the estimated values from the curve fit than the expected values. This would suggest that the expected values are not accurate.

The absorption of blood is based on the amount of haemoglobin and varies between individuals. During the course of the project, blood from different individuals were used. The absorption spectra in Figure 3.2 is based on an average and might not accurately model all blood [27]. In the future, this should be kept in mind when working with phantoms containing blood.

To confirm this hypothesis, a MC simulation was performed to verify the performance of the curve fit. Applying the curve fit on the MC data gave a close to correct result, within a 10 % relative error. However, the result was still limited by diffusion.

The blood used, that was continuously underestimated, probably had a lower haemoglobin concentration than the chromophore spectra in Figure 3.2. Since the error in the phantoms was systematic it could be compensated by multiplying with a correction factor.

Another aspect noticed in the intralipid-blood phantoms was an unknown absorption peak which was present in some of the measurements. This might be some sort of degradation product in blood while it was still fresh.

The agar and Triton-X100 phantoms were created with blood from another specimen, therefore the same kind of analysis was not performed for these phantoms. In the agar phantoms sunflower oil was used, which turned out to be a bad choice of lipid since it barely absorbed any light in the region of interest. The Triton-X100 phantoms containing pig lard were better, but very hard to get homogeneous. Perhaps the results would have been better if agar was used with lard since lard is not a liquid at room temperature and neither is agar. The poor estimation of the lipid volume fraction was probably due to the phantoms inhomogeneity.

Liver

The human liver measurements gave good results, similar to results in reference [47], and were within the region for the diffusion approximation. The reason for the differences in the spectra obtained for patient 2 is not yet established. The result from the pathologist is still pending and will confirm whether the patient's liver was different and/or a measurement error was made.

Measurements from the porcine liver showed the expected loss of water and a higher concentration of fat on the second day of measurement, due to water evaporation. The measurements over the liver were homogeneous and the difference between the two livers small. The porcine liver also had a similar spectra to the human liver.

The murinae livers were all different in size and shape. Because of their small size, light did occasionally escape the organ and thus affecting the acquired signal. These results were not as consistent as for the human and the porcine livers.

Probe Pressure

No difference was noticed for different pressures during the liver measurements, but the measurements were *ex vivo* and the blood flow was severed during the resection. Initially, when the pressure was induced, a difference could be noticed in the real time data on the screen but this quickly subsided.

7.3 CURVE FIT

Some flaws in the curve fit are still present. It was noted that for two seemingly similar spectra and well fitted curve fits, the total summation added up to 100 in one case and only to about 50 in the other. This was due to overestimation of the reduced scattering at the reference wavelength. One way to elude this problem is to implement a constraint to force the total summation of chromophores to 100 % which was also suggested in reference [28].

Another problem with the curve fit is that for the liver measurements the model seems to overestimate bile. From the Monte Carlo simulation with a theoretical value of bile of 5.5 % the curve fit found the bile to be 12.7 % whereas the other chromophores were much closer to the original data, yet underestimated. This might be due to the fact the water absorption and bile absorption are more or less the same for wavelengths in the NIR-region. With several algorithms which focus on different chromophores through weight factors, the robustness of the curve fit could be additionally increased.

The curve fit's residual is highest in the NIR-region. As mentioned, this is probably due to the diffusion approximation. However, another aspect could be the correction factor which adjusts the signal from the NIRQuest-512.

8 CONCLUSIONS

The conclusions of the project are presented and are overall pleasing. After this the outlook of the project and suggestions for further work are presented. Conclusions are drawn in respect to list of the specific aims presented in Chapter 1.

8.1 AIMS

A. Validation

In this thesis, a validation procedure was performed with several probes. For future prospects, this thesis can be used as a guideline to validate other probes, e.g. Probe 3 which was also designed in this project.

Several recipes for phantoms were tested and suggestions on how to improve them included. The different phantoms gave varying result. The blood volume was mostly underestimated due to diffusion limitations and a lack of haemoglobin in the blood. Refined methods are probably needed to mix agar and Triton-X100 phantoms more homogeneously.

B. Curve fit

A curve fit algorithm was developed using a diffusion model, which was tested in tissue phantoms, murinae, porcine and human liver. The results were varying. The livers gave a better curve fit and agreed with data which have been presented by others [26, 47].

C. Interface

The created interface saved a lot of time, both during measurements and especially during the validation and data analysis. The program is easy to use and fulfilled the criteria put up for it. The two window approach with one window for collecting data and one for the analysis helped to keep it minimalistic.

D. Difference between healthy and malignant tissue

There was a noticeable difference between healthy and malignant tissue. These differences were mostly noticed when the measurement was acquired from a visible tumour, but not when the tumour was buried deeper in the tissue. Here the penetration depth limits the result.

E. Probe pressure

The probe pressure did not affect this project since all measurements were made *ex vivo*, but will most likely affect *in vivo* measurements.

F. Limitations with diffusion

Diffusion theory is limited by the fibre separation and also limited where absorption no longer is neglectable compared to scattering, usually above 1300 nm. The theoretical and the experimental results agreed and recognised that the diffusion model has limitations in this application. The results will most likely improve with the arrival of Probe 3 since it is designed with a greater fibre separation.

8.2 OUTLOOK

For the future of this project and the validation of Probe 3 there are several aspects to consider. When mixing phantoms, agar can be tried with pig lard instead of sunflower oil. The lipid particle size shoulds be considered and reduced to make the preparation easier.

For increased robustness, the reference spectrum should be acquired from a fixed distance from the reflective plate. The integration time should also be suitable for the purpose, i.e. the same integration time should always be used in the same application.

For further studies a database of liver spectra can be set up to get a better knowledge of the shape for healthy and malignant tissue. Also, if diffusion proves limited for liver measurements with Probe 3, a MC database can be used for evaluation of acquired spectra.

When measuring *in vivo* the probe pressure should be considered. Both the time elapsed and the pressure itself need to be accounted for in model.

The general model can be extended to other fields and applications within biophotonics.

PERSONAL REFLECTIONS

Therese

During this project I have learned to combine and use knowledge from many different areas to new applications within biophotonics. This is the largest project I have been a part of so far, and I have been able to develop my analytical, programming and logical skills both through my own work and through help from others. It has been beneficial to be a part of the biophotonics group and everyone has been contributing to this project in one way or another. I am happy with the result of this project and hope that it will continue to grow.

David

This has been the largest scientific project I have taken part in. Not only the project itself, but being part of the biophotonic group as a whole has given me great insight on how to work as a team. Though most of the benefits of knowledge have been given to us students, we have also been able to contribute during our weekly meetings and voice our opinions. Furthermore, I have been introduced to how scientific research is performed and the emphasis of systematic, yet easily approached writing.

Workload

Most of the work and much of the research was performed simultaneously by both of us. On the more practical note, Therese focused more on coding the curve fit algorithms and David on the interface along with the real time data from the spectrometers to MATLAB. Therese wrote the majority of chapters 3, and 5 along with the abstract while David wrote most of chapters 2, 4 and 6. The remaining chapters were written by both and the chapters mentioned were also edited by both.

ACKNOWLEDGEMENTS

We would like to thank all of those who have contributed and assisted us in this project. First and foremost, we would like to thank our supervisor Nina Reistad for all the things she has done for us during this project. Both introducing us to the subject of DRS, teaching us and in helping with practical things such as doing some of the Monte Carlo simulations and assisting in preparing some of the illustrations in the thesis.

We would also like to thank our co-supervisors Professor Stefan Andersson-Engels and Johan Axelsson whom both have given us great insight and clarity to problems that arose during the project. Furthermore a declaration to Haiyan Xie and Oskar Vilhelmsson Timmermand for making it possible to do the muraine measurements and to Sören Johansson for assisting us with the Time-of-Flight spectroscopy measurements. People that have helped us at Lund University hospital and those involved in the future of this project: Christian Sturesson, Jan Nilsson, and Sam Eriksson together with Per-Jonas Blind that gave us access.

A special thank you to Elin Kurtsdotter for assisting in some of the illustration work.

And finally, to everyone in the biophotonics group for contributing to a great work environment!

[1] David A Boas, Dana H Brooks, Eric L Miller, Charles A DiMarzio, Misha Kilmer, Richard J Gaudette, and Quan Zhang. Imaging the body with diffuse optical tomography. *Signal Processing Magazine, IEEE*, 18(6):57–75, 2001.

[2] Haiyan Xie. Towards Undistorted Fluorescence for Tissue Diagnostics and Therapy Monitoring. 2014.

[3] Alnawaz Rehemtulla, Lauren D Stegman, Shaun J Cardozo, Sheila Gupta, Daniel E Hall, Christopher H Contag, and Brian D Ross. Rapid and quantitative assessment of cancer treatment response using< i> in vivo</i> bioluminescence imaging. *Neoplasia*, 2(6):491–495, 2000.

[4] Haiyan Cen and Yong He. Theory and application of near infrared reflectance spectroscopy in determination of food quality. *Trends in Food Science & Technology*, 18(2):72–83, 2007.

[5] M Blanco, J Coello, H Iturriaga, S Maspoch, and C De la Pezuela. Quantitation of the active compound and major excipients in a pharmaceutical formulation by near infrared diffuse reflectance spectroscopy with fibre optical probe. *Analytica chimica acta*, 333(1):147–156, 1996.

[6] Matheus P Freitas, Andréia Sabadin, Leandro M Silva, Fábio M Giannotti, Débora A do Couto, Edivan Tonhi, Renato S Medeiros, Gislaine L Coco, Valter FT Russo, and José A Martins. Prediction of drug dissolution profiles from tablets using nir diffuse reflectance spectroscopy: A rapid and nondestructive method. *Journal of pharmaceutical and biomedical analysis*, 39(1):17–21, 2005.

[7] Torre M Bydlon, Rami Nachabé, Nimmi Ramanujam, Henricus JCM Sterenborg, and Benno HW Hendriks. Chromophore based analyses of steady-state diffuse reflectance spectroscopy: current status and perspectives for clinical adoption. *Journal of biophotonics*, 9999, 2014.

[8] Karthik Vishwanath, Kevin Chang, Daniel Klein, Yu Feng Deng, Vivide Chang, Janelle E Phelps, and Nimmi Ramanujam. Portable, fiber-based, diffuse reflection spectroscopy (drs) systems for estimating tissue optical properties. *Applied spectroscopy*, 65(2):206–215, 2011.

[9] Zoya Volynskaya, Maryann Fitzmaurice, Jon Nazemi, Ramachandra R Dasari, Robert Shenk, Abigail S Haka, Kate L Bechtel, Nancy Wang, and Michael S Feld. Diagnosing breast cancer using diffuse reflectance spectroscopy and intrinsic fluorescence spectroscopy. *Journal of biomedical optics*, 13(2):024012–024012, 2008.

[10] David Hsiang, Amanda Durkin, John Butler, Bruce J Tromberg, Albert Cerussi, and Natasha Shah. In vivo absorption, scattering, and physiologic properties of 58 malignant breast tumors determined by broadband diffuse optical spectroscopy. *Journal of biomedical optics*, 11(4):044005–044005, 2006.

[11] George Zonios, Lev T Perelman, Vadim Backman, Ramasamy Manoharan, Maryann Fitzmaurice, Jacques Van Dam, and Michael S Feld. Diffuse reflectance spectroscopy of human adenomatous colon polyps in vivo. *Applied Optics*, 38(31):6628–6637, 1999.

[12] Neda Haj-Hosseini. *Fluorescence Spectroscopy for Quantitative Demarcation of Glioblastoma Using 5-Aminolevulinic Acid*. PhD thesis, Linköping UniversityLinköping University, Biomedical Instrumentation, The Institute of Technology, 2012.

[13] Rami Nachabé, Benno HW Hendriks, Marjolein van der Voort, Adrien E Desjardins, and Henricus JCM Sterenborg. Estimation of biological chromophores using diffuse optical spectroscopy: benefit of extending the uv-vis wavelength range to include 1000 to 1600 nm. *Biomedical optics express*, 1(5):1432–1442, 2010.

[14] Vikramjit Mitra and Jane Metcalf. Functional anatomy and blood supply of the liver. *Anaesthesia & Intensive Care Medicine*, 13(2):52–53, 2012.

[15] Ahmedin Jemal, Rebecca Siegel, Elizabeth Ward, Yongping Hao, Jiaquan Xu, Taylor Murray, and Michael J Thun. Cancer statistics, 2008. *CA: a cancer journal for clinicians*, 58(2):71–96, 2008.

[16] Ahmedin Jemal, Freddie Bray, Melissa M Center, Jacques Ferlay, Elizabeth Ward, and David Forman. Global cancer statistics. *CA: a cancer journal for clinicians*, 61(2):69–90, 2011.

[17] Rebecca Siegel, Carol DeSantis, Katherine Virgo, Kevin Stein, Angela Mariotto, Tenbroeck Smith, Dexter Cooper, Ted Gansler, Catherine Lerro, Stacey Fedewa, et al. Cancer treatment and survivorship statistics, 2012. *CA: a cancer journal for clinicians*, 62(4):220–241, 2012.

[18] Timothy M Pawlik and Michael A Choti. Surgical therapy for colorectal metastases to the liver. *Journal of gastrointestinal surgery*, 11(8):1057–1077, 2007.

[19] Christian Sturesson, Jan Nilsson, Sam Eriksson, Lidewij Spelt, and Roland Andersson. Limiting factors for liver regeneration after a major hepatic resection for colorectal cancer metastases. *HPB*, 15(8):646–652, 2013.

[20] Cancer Research UK. How chemotherapy works. http://www.cancerresearchuk.org/cancer-help/about-cancer/treatment/chemotherapy/about/how-chemotherapy-works, 2013. [Online; accessed 12/08/14].

[21] Edwin W Rubel, Stephanie A Furrer, and Jennifer S Stone. A brief history of hair cell regeneration research and speculations on the future. *Hearing research*, 297:42–51, 2013.

[22] Peter J Kneuertz, Shishir K Maithel, Charles A Staley, and David A Kooby. Chemotherapy-associated liver injury: impact on surgical management of colorectal cancer liver metastases. *Annals of surgical oncology*, 18(1):181–190, 2011.

[23] Luigi Solbiati, Tiziana Ierace, Massimo Tonolini, and Luca Cova. Guidance and monitoring of radiofrequency liver tumor ablation with contrast-enhanced ultrasound. *European journal of radiology*, 51:S19–S23, 2004.

[24] Louis G Henyey and Jesse L Greenstein. Diffuse radiation in the galaxy. *The Astrophysical Journal*, 93:70–83, 1941.

[25] Steven L Jacques. Optical properties of biological tissues: a review. *Physics in medicine and biology*, 58(11):R37, 2013.

[26] Rami Nachabé, Daniel J Evers, Benno HW Hendriks, Gerald W Lucassen, Marjolein van der Voort, Jelle Wesseling, and Theo JM Ruers. Effect of bile absorption coefficients on the estimation of liver tissue optical properties and related implications in discriminating healthy and tumorous samples. *Biomedical optics express*, 2(3):600–614, 2011.

[27] Nienke Bosschaart, Gerda J Edelman, Maurice CG Aalders, Ton G van Leeuwen, and Dirk J Faber. A literature review and novel theoretical approach on the optical properties of whole blood. *Lasers in medical science*, pages 1–27, 2013.

[28] RLP Van Veen, W Verkruysse, and HJCM Sterenborg. Diffuse-reflectance spectroscopy from 500 to 1060 nm by correction for inhomogeneously distributed absorbers. *Optics letters*, 27(4):246–248, 2002.

[29] SH Chung, AE Cerussi, SI Merritt, J Ruth, and BJ Tromberg. Non-invasive tissue temperature measurements based on quantitative diffuse optical spectroscopy (dos) of water. *Physics in medicine and biology*, 55(13):3753, 2010.

[30] Rami Nachabé, Henricus JCM Sterenborg, Benno HW Hendriks, Adrien E Desjardins, Marjolein van der Voort, and Martin B van der Mark. Estimation of lipid and water concentrations in scattering media with diffuse optical spectroscopy from 900 to 1600 nm. *Journal of biomedical optics*, 15(3):037015–037015–10, 2010.

[31] Roberto Reif, Mark S Amorosino, Katherine W Calabro, Ousama A'Amar, Satish K Singh, and Irving J Bigio. Analysis of changes in reflectance measurements on biological tissues subjected to different probe pressures. *Journal of biomedical optics*, 13(1):010502–010502–3, 2008.

[32] JA Delgado Atencio, EE Orozco Guillén, S Vázquez y Montiel, M Cunill Rodríguez, J Castro Ramos, JL Gutiérrez, and F Martínez. Influence of probe pressure on human skin diffuse reflectance spectroscopy measurements. *Optical Memory and Neural Networks*, 18(1):6–14, 2009.

[33] Wenliang Chen, Rong Liu, Kexin Xu, and Ruikang K Wang. Influence of contact state on nir diffuse reflectance spectroscopy in vivo. *Journal of Physics D: Applied Physics*, 38(15):2691, 2005.

[34] Blaž Cugmas, Maksimilijan Bregar, Miran Bürmen, Franjo Pernuš, and Boštjan Likar. Impact of contact pressure–induced spectral changes on soft-tissue classification in diffuse reflectance spectroscopy: problems and solutions. *Journal of biomedical optics*, 19(3):037002–037002, 2014.

[35] Yalin Ti and Wei-Chiang Lin. Effects of probe contact pressure on in vivo optical spectroscopy. *Optics express*, 16(6):4250–4262, 2008.

[36] Haichun Liu. *Advancing Upconversion Emissions for Biomedical Imaging*. PhD thesis, Lund University, 2014.

[37] Thomas J Farrell, Michael S Patterson, and Brian Wilson. A diffusion theory model of spatially resolved, steady state diffuse reflectance for the noninvasive determination of tissue optical properties invivo. *Medical physics*, 19(4):879–888, 1992.

[38] Anthony Kim, Mathieu Roy, Farhan Dadani, and Brian C Wilson. A fiberoptic reflectance probe with multiple source-collector separations to increase the dynamic range of derived tissue optical absorption and scattering coefficients. *Optics express*, 18(6):5580–5594, 2010.

[39] Karin M Asplund, Kenneth A Schenkman, Wayne A Ciesielski, and Lorilee SL Arakaki. Photon path depth in tissue phantoms: a comparison of visible and near-infrared (nir) wavelengths. In *SPIE BiOS*, pages 89450D–89450D. International Society for Optics and Photonics, 2014.

[40] Ocean Optics. USB4000 Data Sheet. http://www.oceanoptics.com/technical/engineering/USB4000%20OEM%20Data%20Sheet.pdf, 2012. [Online; accessed 14/08/14].

[41] Ocean Optics. NIRQuest NIR Spectrometers Data Sheet. http://www.oceanoptics.com/technical/engineering/OEM%20Data%20Sheet%20--%20NIRQuest.pdf, 2014. [Online; accessed 14/08/14].

[42] George Zonios. Noise and stray light characterization of a compact ccd spectrophotometer used in biomedical applications. *Applied optics*, 49(2):163–169, 2010.

[43] Ocean Optics. InGaAs linear image sensor G9301 to G9204. http://www.oceanoptics.com/technical/detectorhahamatsuG9204.pdf, 2006. [Online; accessed 14/08/14].

[44] Urs Utzinger and Rebecca R Richards-Kortum. Fiber optic probes for biomedical optical spectroscopy. *Journal of Biomedical Optics*, 8(1):121–147, 2003.

[45] Ulas Sunar. *Monitoring tumor therapeutic response with diffuse optical spectroscopies*. PhD thesis, University of Pennsylvania, 2006.

[46] Abraham Savitzky and Marcel JE Golay. Smoothing and differentiation of data by simplified least squares procedures. *Analytical chemistry*, 36(8):1627–1639, 1964.

[47] DJ Evers, R Nachabé, D Hompes, F van Coevorden, GW Lucassen, BHW Hendriks, M-LF van Velthuysen, J Wesseling, and TJM Ruers. Optical sensing for tumor detection in the liver. *European Journal of Surgical Oncology (EJSO)*, 39(1):68–75, 2013.

[48] Gerard Downey, Peter McIntyre, and Antony N Davies. Detecting and quantifying sunflower oil adulteration in extra virgin olive oils from the eastern mediterranean by visible and near-infrared spectroscopy. *Journal of Agricultural and Food chemistry*, 50(20):5520–5525, 2002.

[49] A Pifferi, RLP van Veen, HJCM Sterenborg, Alessandro Torricelli, Ekaterine Chikoidze, and Rinaldo Cubeddu. Determination of visible near-ir absorption coefficients of mammalian fat using time-and spatially resolved diffuse reflectance and transmission spectroscopy. *Journal of biomedical optics*, 10(5):054004–054004–6, 2005.

[50] Homa Assadi, Raffi Karshafian, and Alexandre Douplik. Optical scattering properties of intralipid phantom in presence of encapsulated microbubbles. *International Journal of Photoenergy*, 2014, 2014.

[51] Stephen T Flock, Steven L Jacques, Brian C Wilson, Willem M Star, and Martin JC van Gemert. Optical properties of intralipid: a phantom medium for light propagation studies. *Lasers in Surgery and Medicine*, 12(5):510–519, 1992.

[52] Giovanna Quarto, Antonio Pifferi, Ilaria Bargigia, Andrea Farina, Rinaldo Cubeddu, and Paola Taroni. Recipes to make organic phantoms for diffusive optical spectroscopy. *Applied optics*, 52(11):2494–2502, 2013.

[53] Brian W Pogue and Michael S Patterson. Review of tissue simulating phantoms for optical spectroscopy, imaging and dosimetry. *Journal of biomedical optics*, 11(4):041102–041102, 2006.

[54] Anthony J Durkin. Comparison of water and lipid content measurements using diffuse optical spectroscopy and mri in emulsion phantoms. *Technology in cancer research & treatment*, 2(6), 2003.

[55] Sergio E Hernández, Vicente D Rodríguez, Felipe A Martín, Jose Luis Gonzalez-Mora, Miguel A Castellano, and Justo Pérez. Diffuse reflectance spectroscopy characterization of hemoglobin and intralipid solutions: in vitro measurements with continuous variation of absorption and scattering. *Journal of biomedical optics*, 14(3):034026–034026–6, 2009.

[56] Lihong Wang, Steven L Jacques, and Liqiong Zheng. Mcml—monte carlo modeling of light transport in multi-layered tissues. *Computer methods and programs in biomedicine*, 47(2):131–146, 1995.

[57] Tomas Svensson, Erik Alerstam, Dmitry Khoptyar, Jonas Johansson, Staffan Folestad, and Stefan Andersson-Engels. Near-infrared photon time-of-flight spectroscopy of turbid materials up to 1400 nm. *Review of scientific instruments*, 80(6):063105, 2009.

APPENDIX A

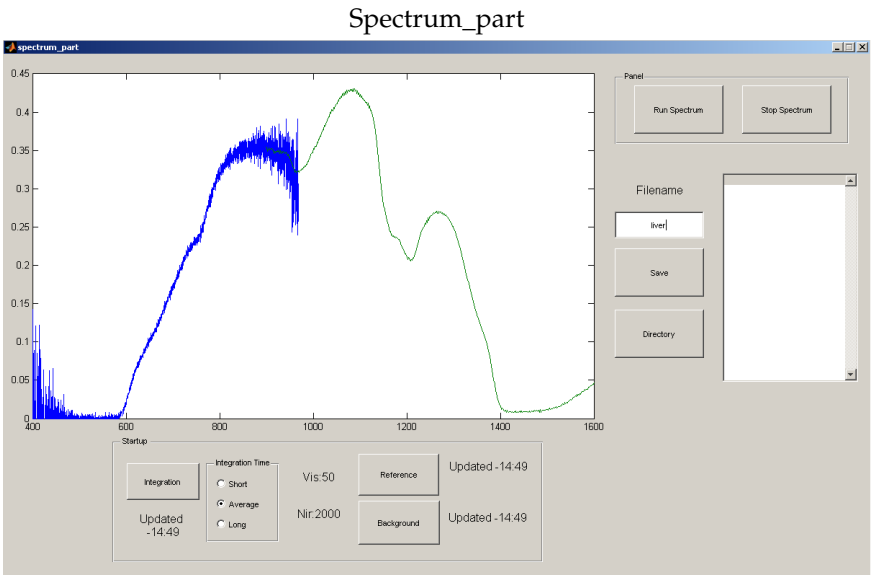

Figure A.1: Interface for running the spectrometers and acquiring spectra. Signal from the USB-4000 (blue) and NIRQuest-512 (green). It is easily noticed that the signal-to-noise ratio is worse for the USB-4000.

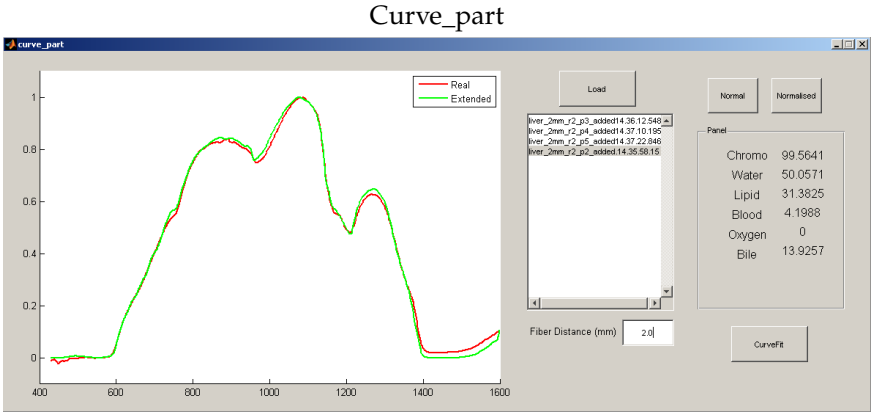

Figure A.2: Interface for analysing the data and performing the curve fit. Signal curve (red) and curve fit (green).